On the bending of MS1-P20 hybrid steels additively manufactured using laser powder bed fusion

Shakerin, Sajad; Sanjari, Mehdi; Pirgazi, Hadi; Amirkhiz, Babak Shalchi; Mohammadi, Mohsen

DOI
10.1016/j.mtla.2022.101501

Publication date
2022

Document Version
Final published version

Published in
Materialia

Materialia 24 (2022) 101501

Contents lists available at ScienceDirect

Materialia

journal homepage: www.elsevier.com/locate/mtla

On the bending of MS1-P20 hybrid steels additively manufactured using laser powder bed fusion

Sajad Shakerin[a,*], Mehdi Sanjari[a,b], Hadi Pirgazi[c,d], Babak Shalchi Amirkhiz[b,a], Mohsen Mohammadi[a]

[a] Marine Additive Manufacturing Centre of Excellence (MAMCE), University of New Brunswick, Fredericton, NB, E3B 5A1, Canada
[b] CanmetMATERIALS, Natural Resources Canada, 183 Longwood Road South, Hamilton, ON, L8P 0A5, Canada
[c] Department of Electromechanical, Systems & Metal Engineering, Ghent University, Ghent, Belgium
[d] Department of Materials Science and Engineering, Delft University of Technology, Delft, the The Netherlands

ARTICLE INFO

Keywords:
Additive manufacturing
Hybrid steel
Interface
Heat treatment sequence
Bending tests
Uniform deformation

ABSTRACT

Maraging steel (MS1)-tool steel (P20) bimetals additively manufactured using the laser powder bed fusion technique were studied under different heat treatment cycles and loading conditions. The hardening of P20 and aging of MS1 were performed sequentially on the hybrid samples. The interfacial characteristics and microstructural evolution of the bulk materials were studied using various advanced electron microscopy techniques. The post-processing procedures successfully produced a uniform martensitic structure throughout the MS1-P20 hybrid steels, leading to a less detectable interface under electron backscatter diffraction (EBSD) imaging. The mechanical performance of heat-treated hybrid steels was evaluated using complex loading conditions. 3-point and 4-point bending tests were performed to assess the impact of heat treatments on the mechanical performance of the hybrid steels. The heat-treated samples exhibited higher strength with relatively homogeneous hardness variations and deformed more uniformly in bending conditions.

1. Introduction

Metal additive manufacturing (MAM) technologies have been restructuring the concept of manufacturing and establishing new infrastructure for the next generation of metal part productions. Many engineering challenges are being facilitated in the production of advanced materials as well as intricate shapes. Most industries are now benefiting from the novel opportunities that MAM can offer them. As an illustration, complex alloys, functionally graded materials, and miniature structures were produced using MAM methods for marine applications [1–6]. In the aerospace industry, extensive research has been conducted, where lighter materials with superior efficiency were manufactured at lower costs and lead time [7,8]. Many alloys such as titanium, nickel, aluminum alloys, and many grades of steels and stainless steels were also processed via the MAM platform, and unique microstructures with superior properties were achieved [9–17].

In today's manufacturing world, the concept of novel materials is becoming significant due to complex working conditions growing daily. This requires new ideas for processing raw materials to create innovative compounds. Of those innovations, bimetals have overcome the limitations of conventional alloys and brought new capabilitieston engineering applications [18]. However, conventional manufacturing techniques cannot fully provide satisfactory conditions to produce bimetals. For instance, welding procedures have been extensively used, but defects such as HAZ, solidification cracking, and embrittlement are unavoidable. Instead, MAM has recently introduced a practical approach tomanufacturinge these materials due to the layer-by-layer buildup of feedstock materials inherent in additive manufacturing.

Steel-bronze, Inconel-stainless steel, 17–4 pH-316 L, Fe-Al12Si, and Ti6Al4V-IN718 are some recent examples of bimetals that were prepared fully via additive manufacturing [19–23]. The bimetallic systems can also be manufactured using a hybrid approach [24]. In this case, a conventionally manufactured alloy is used as a substrate, and then a powder feedstock is deposited on top of it. This is called hybrid additive manufacturing (HAM), which combines subtractive manufacturing or forming methods with the MAM techniques [24]. Several HAM bimetallic systems were studied recently, including Ti6Al4V-316 L, AlSi10Mg-AA2618, NAB-316 L, and steel-steel [25–30].

Since bimetals usually involve two dissimilar metal components, various alloy combinations have been studied for this purpose. Thus, the bimetallic systems of interest can become widely diverse, and each case requires detailed research. Of particular importance is an MS1-P20 system as a new maraging steel bimetal with potential applications in the tool and die industry. The P20 steel is a low-alloy tool steel with rela-

* Corresponding author.
E-mail address: sshakeri@unb.ca (S. Shakerin).

https://doi.org/10.1016/j.mtla.2022.101501
Received 11 April 2022; Accepted 1 July 2022
Available online 2 July 2022

Table 1
Specification of the raw materials; alloying elements are in weight percentage (wt.%).

Maraging steel MS1 powder									
C	Ni	Co	Mo	Ti	Mn, Si	Al	Cr, Cu	P, S	Particle Diameter
≤0.03	17–19	8.5–9.5	4.5–5.2	0.6–0.8	≤0.1	0.05–0.15	≤0.5	≤0.01	$1-45\ \mu m$

As-received P20 block					
C	Mn	Cr	Si	Mo	Dimension
0.28–0.40	0.60–1.00	1.40–2.00	0.20–0.80	0.30–0.55	$150 \times 70 \times 100\ mm^3$

Table 2
Electron microscopy techniques and equipment are used to study MS1-P20 hybrid steels.

Scanning Electron Microscope (SEM)			Transmission Electron Microscope (TEM)	
Microscope	Detector		Microscope	Detector
Thermo Fisher Scientific / FEI Scios 2	EDS Oxford Energy Dispersive Spectrometer	EBSD Oxford Symmetry	FEI Tecnai Osiris	EDS Brucker quad-core X-ray EDS

tively high strength, superior hardness, and acceptable toughness. The P20 tool steel is extensively used in low-temperature tooling applications, including plastic injection molds, extrusion, and die casting dies. Due to severe working conditions, early surface degradation can occur in P20 dies. The conventional solution is to use surface treatments to obtain appropriate hardness [31], but this only affects the surface properties, and the bulk properties remain the same. One can suggest printing the P20 tool steel to produce the whole part with additive manufacturing; however, the high carbon content of P20 can cause brittleness and limit the AM process [32]. Another solution would be using the AM bimetal approach in which a harder material can be deposited on top of P20. This approach can substantially increase hardness and strength in the die, and more complex shapes can be created for die cavities eliminating the need for conventional machining methods. In addition, pre-design cooling channels can be included inside the dies, which is not feasible by the conventional means. Therefore, the bimetal approach can prevent die degradation and cause more unique features. One of the main criteria for producing a successful bimetal component is selecting the appropriate material for deposition. In this regard, maraging steel is the material of interest due to its printability, high ductility, and mechanical strength [33,34]. This bimetal involves a conventionally made P20 steel and an additively manufactured maraging steel (MS1) called the MS1-P20 hybrid steel.

One of the most investigated bimetals is maraging steel bimetals since maraging steel is a material of interest in laser powder-based MAM techniques [35–38]. It was reported that a free-defect interface with excellent mechanical strength is the key characteristic of maraging steel bimetals, making them ideal candidates for high-temperature applications [30,39–42]. Recently, MS1-H13 bimetals were produced using the laser powder bed fusion (LPBF) technique, where different post-processing techniques were employed to homogenize their interfacial characteristics [39,43]. The effect of different heat treatment procedures on maraging steel-based bimetals was studied by other researchers as well; see, e.g. [44,45].

Most maraging steel-based bimetals manufactured for the tool and die application are associated with severe working conditions, where complex loadings exist. Most studies available in the open literature on these AM bimetals were focused on the typical uniaxial tensile behavior, which involves the simplest loading condition, unlike the service conditions. Only a few examples can be found, including the flexural test on 316L-Hastelloy X and Al10SiMg-C18400 bimetals [46,47]. Flexural testing regimes can generate loading conditions in both tension and compression situations that can simultaneously occur on a specimen. Therefore, this work considered both types of flexural tests, including the three-point (3P) bending and four-point (4P) bending, for AM MS1-P20 hybrid steels. This way, a more sophisticated evaluation of the mechanical properties using 3P and 4P bending tests were proposed. In addition, most bimetals involve dissimilar alloys with vastly different chemical compositions, and microstructures can possess unbalanced mechanical properties, negatively affecting their performance. Therefore, modifying the microstructural characteristics of MS1-P20 hybrid steels via proper heat treatment sequences was investigated in this work. The microstructural profile across the AM MS1-P20 hybrid steel interface was customized using the heat-treating procedures. The ultimate goal of this work is to manufacture an MS1-P20 bimetal part with homogenized microstructure and uniform properties that can exhibit acceptable performance under complex loading conditions.

2. Experimental procedure

Two dissimilar materials were used for manufacturing the MS1-P20 hybrid steel: an as-received P20 block as the build plate and maraging steel MS1 powder as the feedstock material. The specifications of these two alloys are shown in Table 1. The P20 block was received in the annealed condition from the manufacturer. The hybrid steel was manufactured using the LPBF process. For this purpose, an EOS M290 additive machine was utilized, which features a Yb-fiber laser with maximum laser power of 400 W. Here, the laser power was set to 285 W during the process. The P20 block was screwed to the additive machine and preheated to 40 °C. The printing chamber was filled with an argon gas (99.9% purity) to avoid oxidation during the LPBF process. The first MS1 powder layer with a thickness of 40 μm was uniformly spread on the P20 build plate. The laser started scanning and fusing the powder layer at a speed of 960 mm/s. The laser scanning was pursued with a strip-like strategy, and the laser beam rotated 67° after completing each individual layer. The hatch distance and spot sizes were 0.11 mm and 100 μm, respectively. The maraging steels were deposited vertically as round bars on top of the P20 plate with the dimension shown in Table 2. The final round bar samples were carefully extracted from the additive machine and cut for the heat treatment procedure, as shown in Fig. 1. Two heat treatment sequences were carried out which are as follows: 1) HT treatment at 880 °C for 1 hour + air cooling and 2) HAT treatment at 880 °C for 1 hour + air cooling + heating at 500 °C for 2 h + air cooling. The MS1-P20 samples were correspondingly classified as-built (AB), hardening treated (HT), and hardening and aging treated (HAT). The heat treatment cycles were carried out by heating the samples in an argon-controlled furnace, and then air cooling was performed to the room temperature.

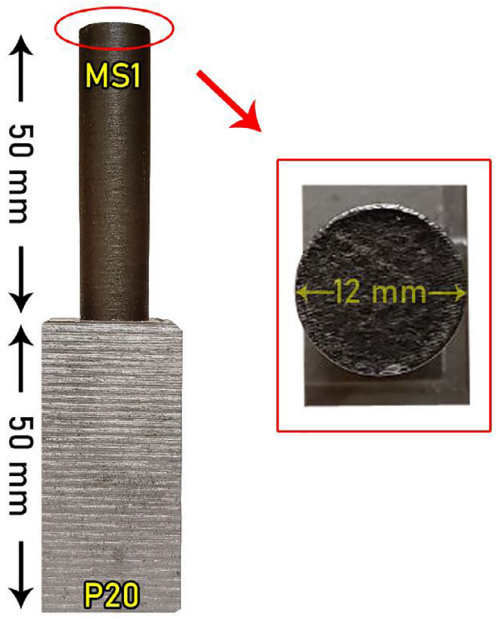

Fig. 1. Dimension of round bar MS1-P20 hybrid steel.

The microstructural samples were sectioned across the boundary between P20 and MS1 and were polished for electron microscopy investigations. Table 2 shows three types of electron microscopy techniques used to develop a comprehensive vision of various aspects of the produced microstructure. The electron backscatter diffraction (EBSD) data was collected via Aztec software, and data processing was carried out using HKL Channel 5 and OIM softwares. The prior austenite grains (PAGs) were reconstructed from the AB, HT, and HAT samples based on the approach proposed in [48,49]. TEM microscopy requires a particular sample preparation, so the focus ion beam (FIB) milling technique was carried out via an FEI Helios Nanolab 650 dual-beam system. Several microhardness tests were also conducted on the microstructural samples. A Vickers microhardness machine was utilized, in which the indenter loading and strain rate were set to 50 mN and $0.2s^{-1}$, respectively.

The bending tests were conducted in two different formats according to ASTM E290 Standard [50]: 1) three-point (3P) bending and 2) four-point (4P) bending tests. A specific fixture was designed and fabricated for each test as illustrated in Fig. 2. The round bar samples were machined to cubic shapes, where the interface was located at the center. Both bending tests were performed at a constant crosshead speed of 5 mm/min, and the data were collected as force-displacement plots. The bent samples were also sectioned at the interface and used for further microscopy via EBSD and TEM.

3. Results

3.1. Heat treatment selection

The fabricated MS1-P20 hybrid steel consists of two different materials, and this difference can lead to more complicated criteria for heat treatment. Thus, the following strategy was used as the selection criteria. The typical heat treatment cycles for MS1 and P20 were first evaluated, and identical cycles were designed and carried out on both materials. The microhardness test was then conducted to select the appropriate heat treatment for the MS1-P20 hybrid steel. P20 mold steel can be commonly hardened within the temperature range of 850–880 °C and tempered within 200–600 °C [51]. For MS1, the temperature ranges of 800–900 °C and 400–600 °C were reported as the solution and aging treatments, respectively [52]. Thus, the P20 hardening temperature of 880 °C and MS1 aging temperature of 500 °C were considered for the MS1-P20 hybrid steel.

Fig. 3 illustrates the microhardness variation for the as-built and heat-treated samples. The as-built sample involves a very soft substrate of 325 HV as expected and a very hard area of 475 HV right above

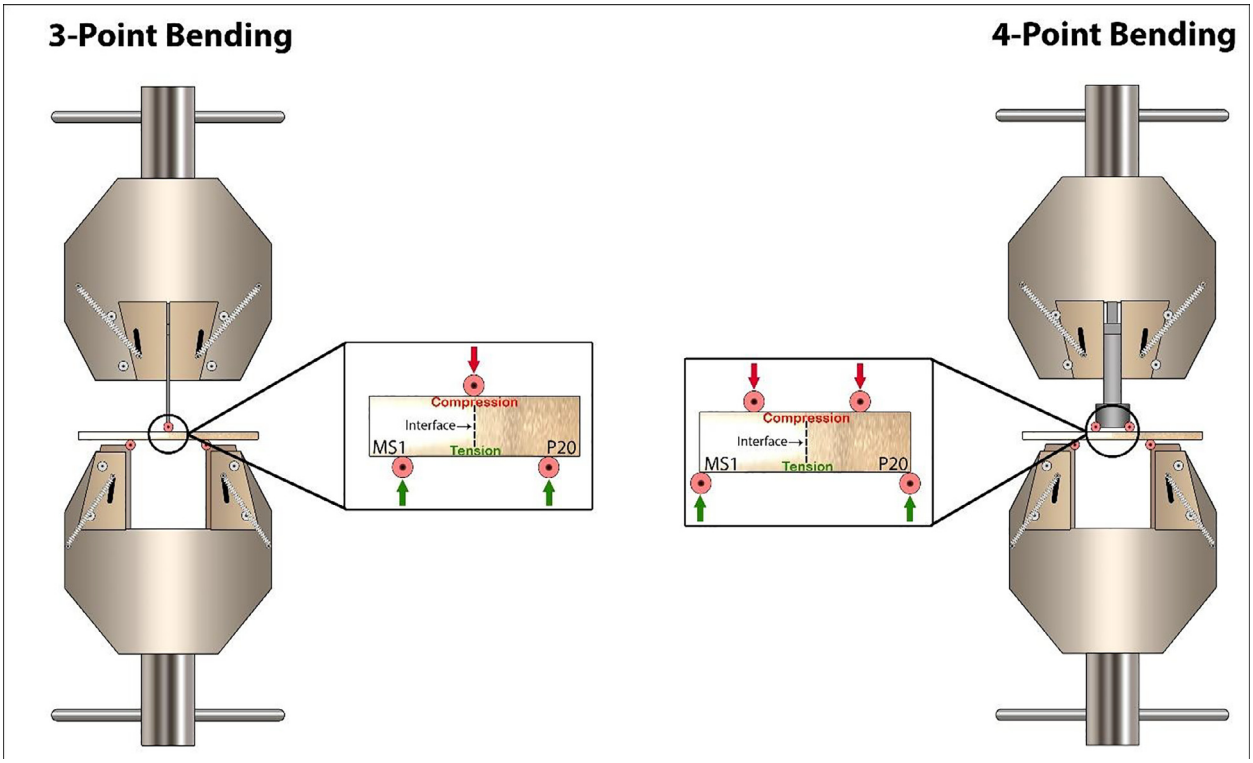

Fig. 2. Schematic of three-point (3P) and four-point (4P) bending tests.

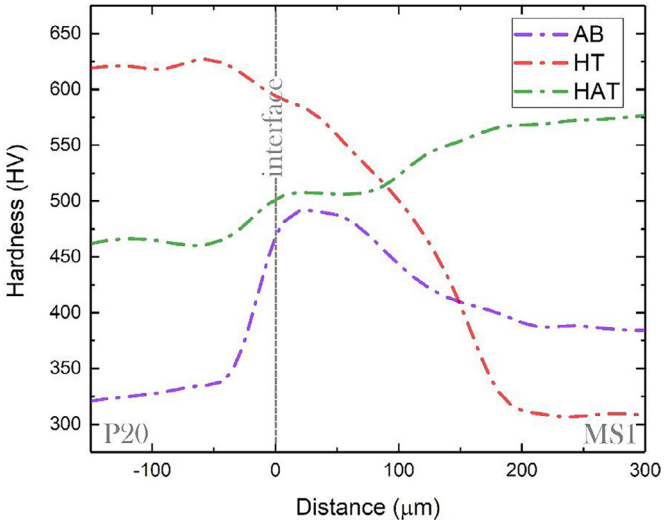

Fig. 3. Microhardness gradient across the MS1-P20 interface.

the interface. In as-built sample, the hardness values of P20 and MS1 are within the range of the literature [39,53]. The hardness decreases below 400 HV, reaching the hardness value of as-built MS1. In HT condition, the average hardness escalated to 625 HV in P20 due to the effect of martensite hardening, and then a sharp drop occurred from the interface to MS1, which was softened with values around 300 HV. In HAT, the hardness values drop in the substrate, while there is a remarkable rise in hardness of the additive side with respect to the HT-sample. Despite the extreme variation of hardness in AB- and HT- samples, the HAT-sample exhibited a relatively homogeneous hardness gradient from P20 to MS1. The hardening followed by aging treatment (HAT) can produce more uniform properties than HT treatment; therefore, the HAT-sample was selected for further investigations.

3.2. Heat-treated bulk materials

The HAT sequence's microstructural effect on MS1 and P20 bulk materials is investigated via SEM and presented in Fig. 4. The as-built MS1 (AB-MS1) contains a hierarchical structure, where groups of ultrafine solidification cells form a grain (see Fig. 4(a)). However, the HAT sequence removed the solidification structure of MS1 and seemed to form some fine precipitates (see Fig. 4(b)). The same analysis was carried out on P20 in AB and HAT conditions, as presented in Figs. 4(c) and (d). The as-received P20 (AR-P20) was filled with rough precipitates, mainly Cr-rich and Mn-rich carbides [54]. These precipitates seem to become refined upon the HAT sequence within the P20 grains (see Fig. 4(d).

Figs. 5(a)-(b) illustrate the BD-IPF maps of MS1 before and after the heat treatment. The additive MS1 did not exhibit any dominant color in the IPF maps. The corresponding pole figures confirm that there is no preferred orientation; thus, the heat treatment did not cause any texture in MS1. The IPF maps also indicate that a considerably coarse grain morphology can be developed via the HAT sequence in MS1. The grain boundary maps are also shown in Figs. 5(c)-(d) to illustrate the grain boundary evolution. The grain boundaries can be categorized as very low angle boundaries (VLAB) with rotation angles less than 5°, low angle boundaries (LAGB) of 5–15° misorientation angle, and high angle grain boundaries (HAGB) with misorientations above 15° [55].

The VLABs represent strain energy inside grains, and the total length of VLABs decreased from 8.02 cm to 5.42 cm upon the HAT sequence, indicating that MS1 is relatively in less strain energy state than the as-built condition. LAGBs mark the subgrain structure in green color, where a higher fraction of LAGBs was formed in the heat-treated sample. The HAT sequence increased the total length of LAGBs almost six times the as-built value from 1.43 cm to 9.97 cm. The as-built MS1 contains longer

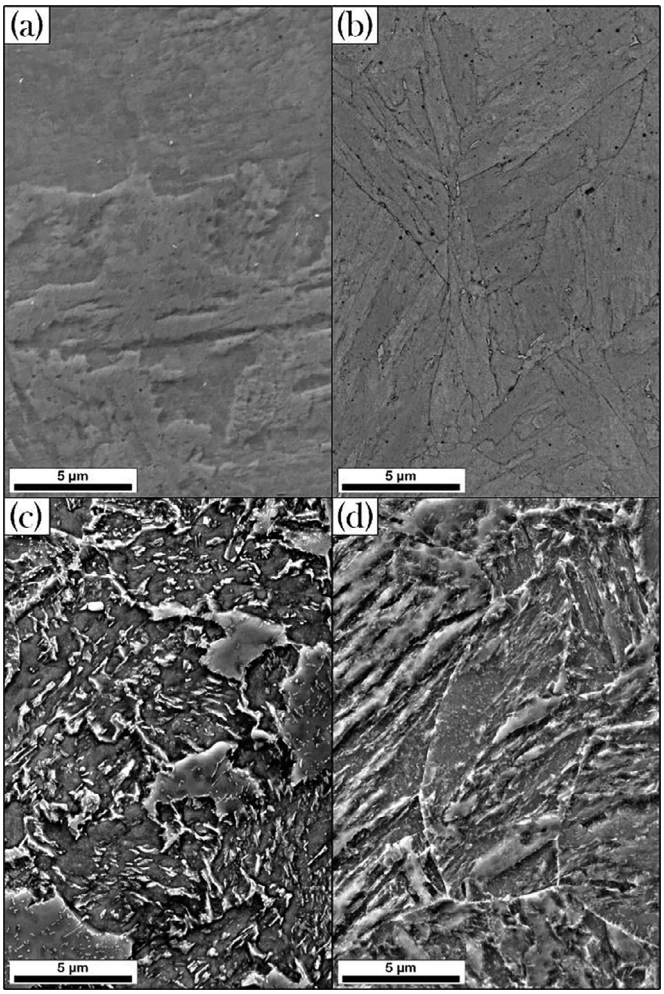

Fig. 4. SEM micrograph of bulk materials: a) as-built MS1 b) HAT-MS1 c) as-received P20 d) HAT-P20.

HAGBs of 3.06 cm compared to 1.94 cm in the HAT-MS1 due to more refined grains of the as-built MS1. Figs. 5(e)-(f) demonstrate the grain size distribution and aspect ratio, respectively. The quantitative values of these two figures are also presented in Table 3. In Fig. 5(e), the AB profile shows an uneven distribution of grains, while the grain area distribution seems uniform since the HAT profile shows a typical Gaussian distribution. Thus, the HAT sequence caused a homogenous grain morphology in MS1. In addition, this heat treatment sequence caused a grain growth from 98.50 μm^2 to 106.03 μm^2 in the printed MS1. The aspect ratio graphs shown in Fig. 5(f) indicate that most grains are equiaxed in both conditions. There is not much difference in fraction values of columnar to equiaxed grains calculated in Table 3.

The grain analysis of P20 was carried out via EBSD and presented in Fig. 6. The BD-IPF map of as-received P20 shows a relative dominancy of blue colors in the [111] direction, and the corresponding pole figure proves the high density of poles for [111] planes (Fig. 6(a)). It seems that the P20 substrate contained a texture in the as-received condition.

Table 3
MS1 grain specification before and after heat treatment.

Sample	Grain Area(um2)	Aspect Ratio (%)		KAM(°)
		Columnar	Equiaxed	
AB	98.50	12	88	1.17
HAT	106.03	16	84	0.86

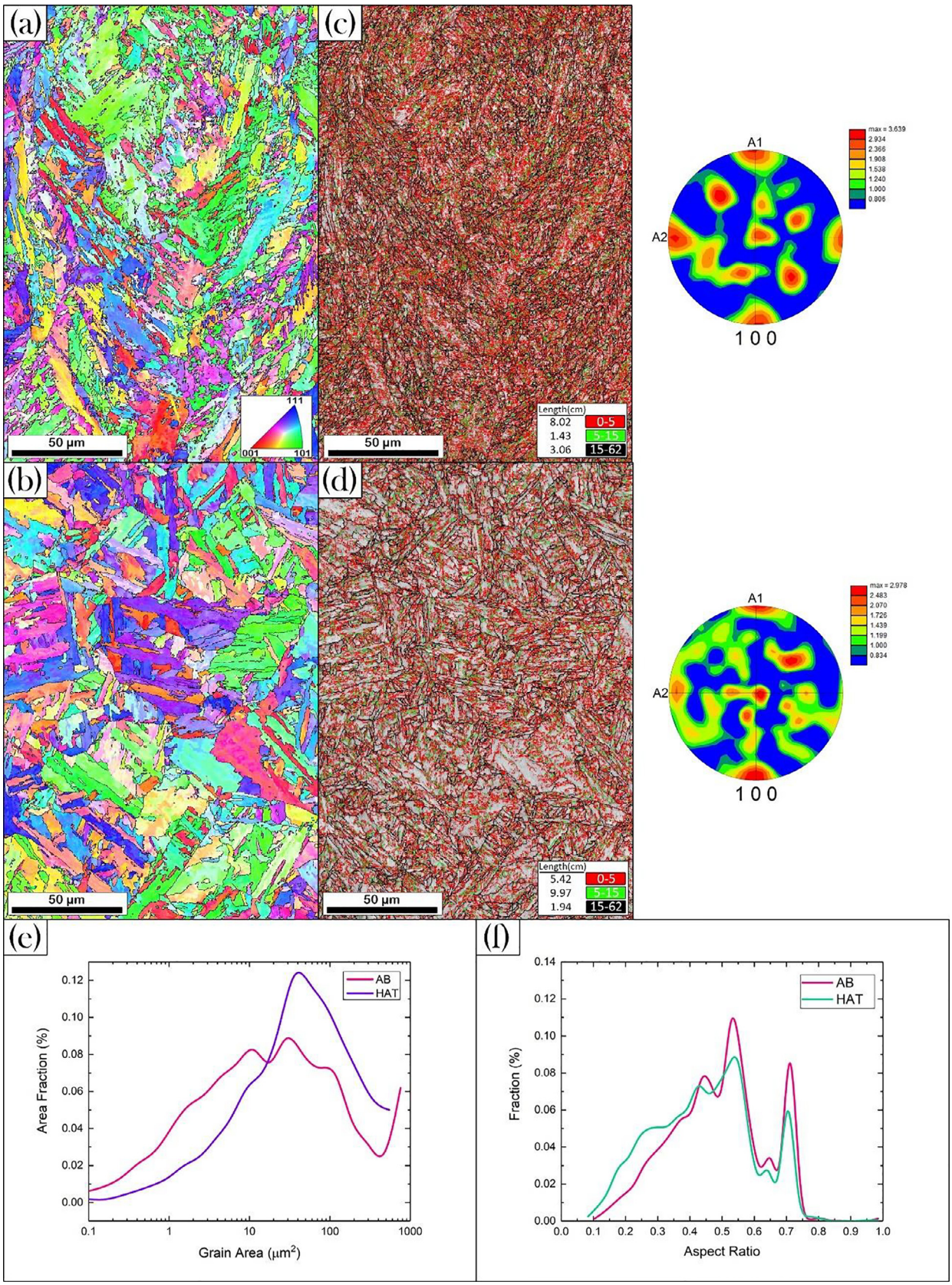

Fig. 5. Grain analysis of MS1; BD-inverse pole figure: a) AB d) HAT; Grain boundary map and corresponding pole figure: c) AB d) HAT; e) grain size distribution; f) Grain aspect ratio.

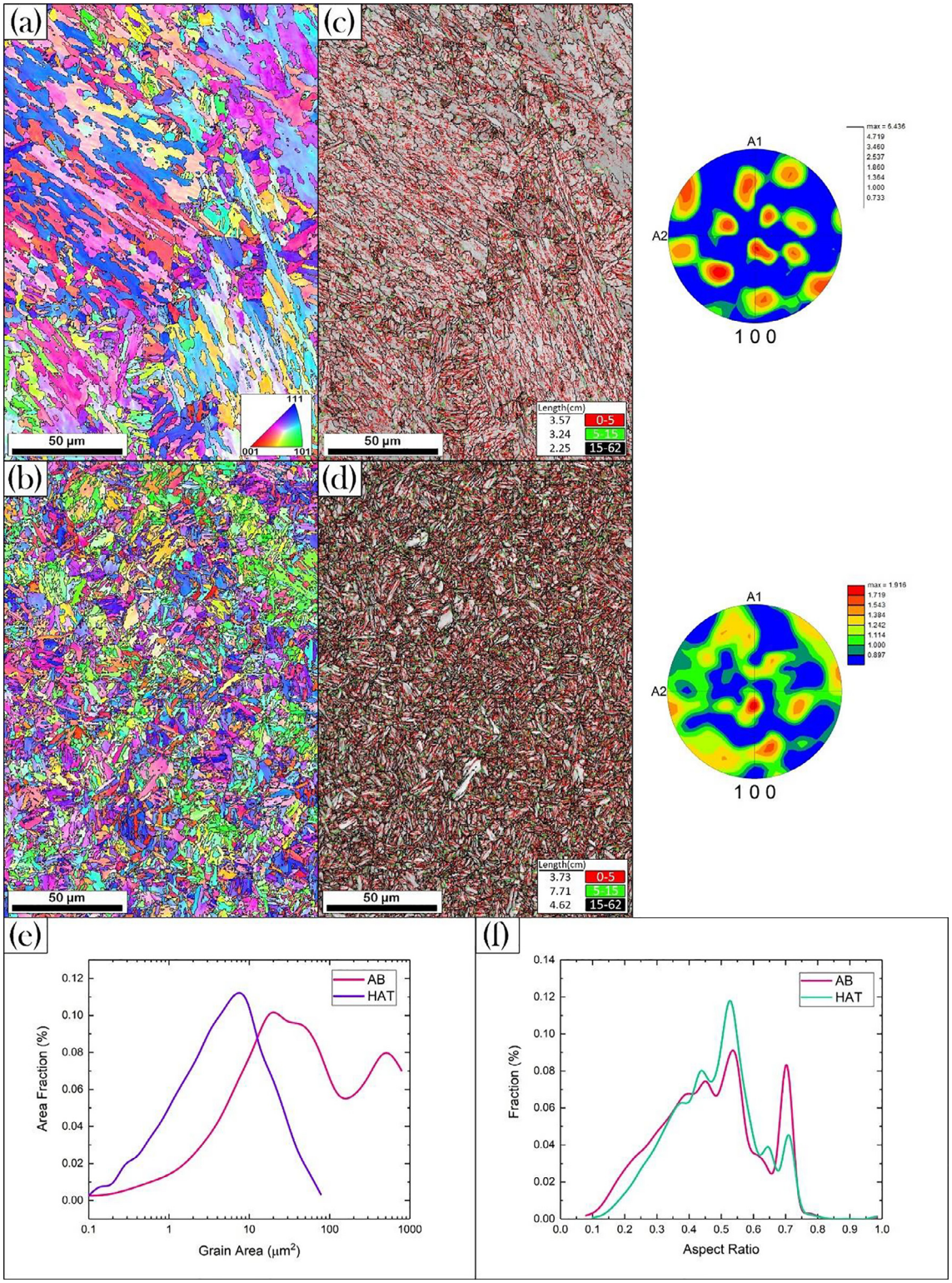

Fig. 6. Grain analysis of P20; BD-inverse pole figure: a) AB d) HAT; Grain boundary map and corresponding pole figure: c) AB d) HAT; e) grain size distribution; f) Grain aspect ratio.

This texture, however, was removed when the HAT sequence was applied to the P20 steel since the IPF map of Fig. 6(b) shows a random color distribution, and the corresponding pole figure indicates a low value of 1.916 MRD (multiples of random density) as the maximum intensity. Regarding grain boundaries, HAGBs, as well as LAsGBs, almost doubled after the HAT sequence, whereas VLABs remained the same (see Figs. 6(c)-(d)). The HAT sequence refined the grains and formed a more profound subgrain structure within P20.

Fig. 6(e) clearly shows that the as-received P20 contains two main peaks, including coarse and very large grains, while the HAT-P20 peak is located within much lower values. In addition, the HAT profile is demonstrated as a normal distribution; thus, the grains seem uniform

Table 4
P20 grain specification before and after heat treatment.

Sample	Grain Area(um2)	Aspect Ratio (%)		KAM(°)
		Columnar	Equiaxed	
AB	160.29	13	87	0.69
HAT	8.88	12	88	0.71

in P20. In other words, Fig. 6(e) is indicative of grain refinement and grain size homogenization upon the HAT sequence in P20. The average grain area for the AB and HAT conditions was calculated to be 160.29 μm^2 and 8.88 μm^2, respectively (see Table 4). In terms of aspect ratio, no tangible change was observed after heat treatment, and the majority of grains remained equiaxed within P20 (see Fig. 6(f)).

3.3. Heat-treated interface

Fig. 7 shows the SEM micrograph of the MS1-P20 interface in the as-built and heat-treated conditions, as well as EDS line analysis across the samples. The AB-sample contains coarse ferritic grains on the substrate side, and a few fractions of solidification cells with the trace of the Marangoni effect can only be seen on the additive side (see Fig. 7(a)). Fig. 7(b) shows the MS1-P20 interface after the HAT sequence, where the substrate underwent martensite transformation. Although the microstructure of the additive side is no longer visible, it can be concluded that the HAT sequence removed the Marangoni effect above the interface. Fig. 7 also presents the profile of the main alloying elements across the interface area. Ni and Co are the MS1 alloying elements, and Cr and Mn are the main alloying elements of P20.

Overall, an ascending gradient for Ni, Co, and a descending gradient for Cr, Mn at the interface indicates the transition zone (TZ). The elemental gradients look identical in both AB and HAT conditions and do not vary significantly. However, there is a remarkable rise in Ni and Co concentrations and a Cr decrease in the HAT-interface. This is the explicit indication of diffusion associated with heat treatment at the interface, where the elemental variations are prominent.

Fig. 8 shows the band contrast and BD-IPF maps of MS1-P20 interfaces before and after heat treatment. The band contrast maps distinguish different areas across the interface. Based on grain size variation, three main areas can be observed: substrate, transition zone (TZ), and fully MS1 zone. In the as-built condition, the interface emerged by very fine grains of TZ solidified on top of large grains of the substrate. The transition zone (TZ) continued to grow about 150–200 μm, and then the maraging steel smoothly appeared above TZ, as highlighted in Fig. 8(a).

Since very fine grains were developed on the substrate, the interface seems highly distinguishable in the as-built condition. The heat-treated interface, however, seems less detectable due to the remarkable grain refinement of the substrate, as can be seen in Fig. 8(b). The heat-treated TZ seems coarser than the as-built one, but the grain growth is more noticeable on MS1 after heat treatment. Figs. 8(c)-(d) demonstrate the grain orientation in terms of inverse pole figures along the building direction. Random color distribution can be easily detected across the interface in both conditions, so no texture was developed in the HAT sequence. Interestingly, the grain contrast seems faint at the HAT-interface since the grain size difference is subtle between P20 and TZ (see Fig. 8(d)).

Fig. 9 represents the strain analysis of the interface in terms of kernel average misorientation (KAM) and grain orientation spread (GOS). The KAM maps demonstrate the stored strain energy inside grains associated with dislocation density [56,57]. In contrast, GOS measures an average value and assigns a color to an individual grain as an indication of strain [58–60]. Figs. 9(a)-(b) reveal the apparent distinction between the substrate and additive side. The additive side is usually highlighted in a brighter color; thus, KAM mapping can be a good candidate for recognizing the interface area.

The GOS maps also display the average misorientation value of each grain. In the AB-interface area, TZ contains lower GOS values than P20 and MS1 since the blue grains are considerable in this area. There exists a non-uniform distribution of GOS misorientation across the interface (see Fig. 9(c)). The heat-treated interface, however, seems more homogeneous in this regard (see Fig. 9(d)).

The MS1-P20 interface features a very fine morphology; thus, further investigations are necessary at higher magnifications. Fig. 10(a) shows the SEM micrograph of the HAT-sample at 5000X, where the morphology contrast between the transition zone and P20 forms the interface. The P20 microstructure is clearly detected with martensitic grains, and very fine precipitates are embedded within the grains. The transition zone (TZ) no longer involves the solidification structure of as-built condition, and interestingly very fine precipitates can be observed. High magnification EBSD mapping of the HAT-interface is shown in Fig. 10(b), where the grains are randomly orientated across the interface. A smooth transition can also be seen in terms of grain size, in which coarser grains turn to finer grains by approaching TZ. Fig. 10(c) also shows the grain boundary morphology of the HAT-interface. Likewise, the coarse-to-fine transition of grains can also be viewed in this figure since more VLABs, LAGBs, and HAGBs were accumulated in TZ rather than P20.

The very fine precipitates of the HAT-interface detected in high-magnification SEM imaging require precise analysis using the TEM/EDS technique. Fig. 11 illustrates the elemental mapping of the HAT-sample right at the interface. This figure reveals the ultrafine details of the interface on the nanoscale. The HAT-interface constitutes a very narrow band of few nanometers between P20 and TZ. Ni and Co, as the main alloying elements of MS1, coexist on both sides of the interface, which confirms the diffusion induced by heat treatment and it caused the enrichment of the interface with these two elements. Hence, the HAT-interface is a Ni-and Co- rich solid solution. In addition, nano precipitates rich in Cr, Mn, and C were accommodated along the interface; thus, Cr and Mn carbides can be considered the other constitution of the HAT-interface. Another type of precipitate can also be seen near the interface, mainly in TZ. These precipitates are AlTi intermetallic compounds reported in AM maraging steel [61]. It seems that the MS1 alloying elements constructed the interface matrix, and the P20 alloying elements pinned the interface by forming nano precipitates. Therefore, superior mechanical properties can be expected for the HAT-interface.

3.4. Flexural performance of MS1-P20 hybrid steel

The mechanical performance of the MS1-P20 hybrid steel was assessed under complex loading conditions. Accordingly, three-point (3 PB) and four-point bending (4 PB) tests were applied to both AB and HAT specimens. Figs. 12(a)-(b) demonstrate the load-displacement curves for 3 PB and 4 PB tests, respectively. The three-point test was performed until the specimen failed at the bottom, where a crack propagated as a result of tension stresses. In 3 PB, the AB-sample started to deform plastically at a lower load (750.86 MPa) and underwent more displacement before failure at 1405.94 MPa. In contrast, the HAT-sample yielded at 993.38 MPa, failed at higher loading (2022.98 MPa), and showed lower displacement with respect to the AB-sample. Thus, the bending strength increased upon heat treatment. Fig. 12(b) similarly shows an identical trend in the 4P-bending test in which the hybrid steel performed stronger after the HAT sequence. Apparently, the HAT sequence effectively enhanced the MS1-P20 hybrid steel under bending conditions. The lower strength values were obtained in 4P-bending than in 3P-bending, which can be attributed to the more complex loading conditions of the 4P-bending test.

Since deformation is associated with the movement and interaction of dislocations, TEM images were taken to study the deformation mechanism at very high magnification. Fig. 13 shows The TEM micrographs of the HAT-sample underwent the four-point bending test. The TEM sample was extracted from the bottom of the bulk specimen and far from the

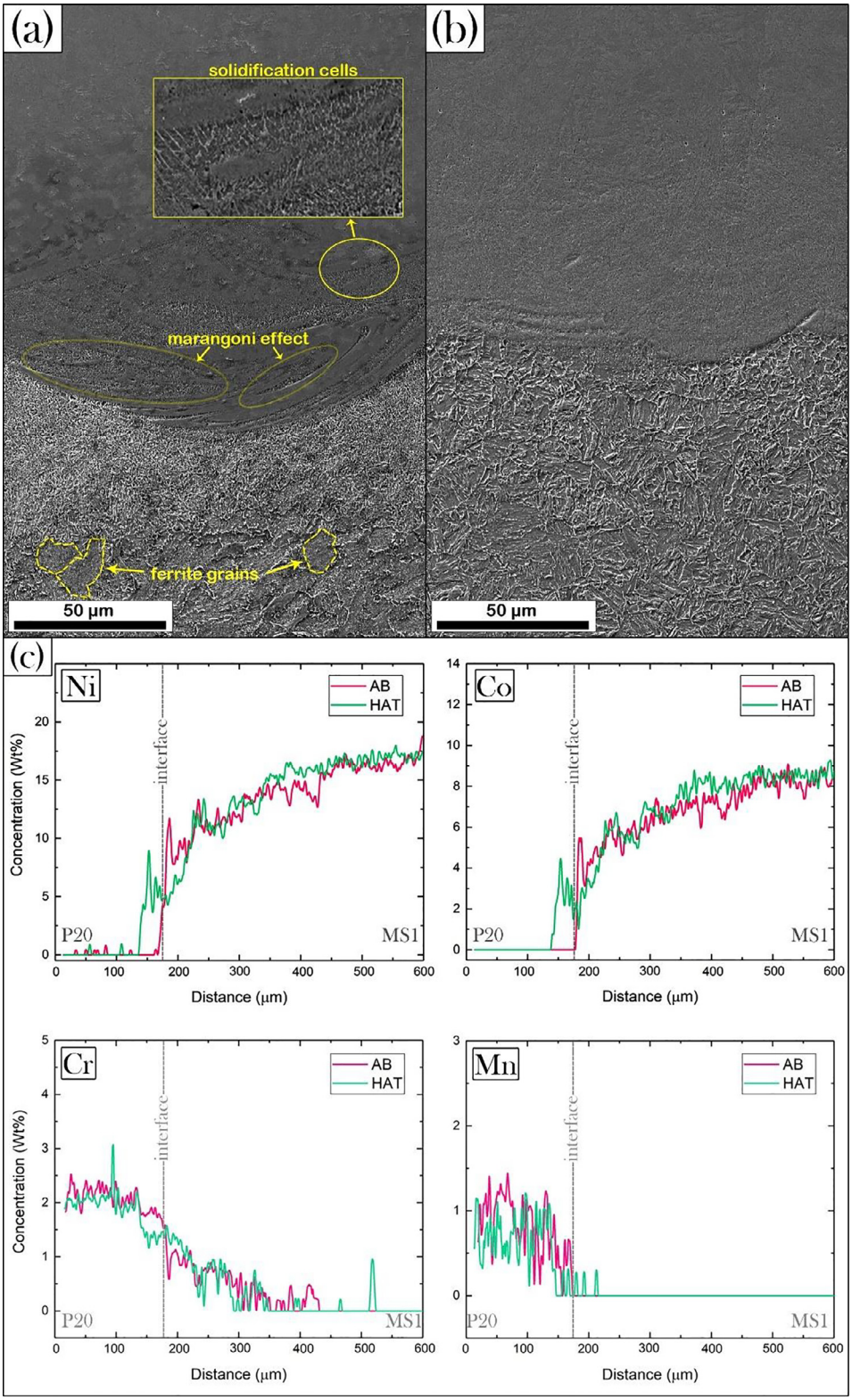

Fig. 7. SEM interfacial micrograph of MS1-P20: a) AB b) HAT; c) EDS elemental variation across the interface for Ni, Co, Cr, and Mn elements.

neutral axis. Fig. 13(a) shows the martensitic lath structure of the HAT-sample as well as the accumulation of dislocations. The dislocations tend to pile up and accumulate through the martensite laths. The individual dislocations can be detected at higher magnification, as shown in Fig. 13(b). The individual dislocations tend to interact with each other and interlock as deformation proceeds. Moreover, the surrounding areas of nano precipitates are depleted in dislocations, which means the strain field of precipitates inhibits the movement of dislocations.

4. Discussion

The heat treatment procedure was proved to significantly impact the MS1-P20 hybrid steel. This section discusses the microstructural modifications which led to the enhancement of mechanical properties.

The MS1-P20 hybrid steel was presented as two-phase steel; martensitic MS1 on ferritic substrate P20 in the as-built condition. Since the martensite phase is harder than ferrite, hardness varies substantially

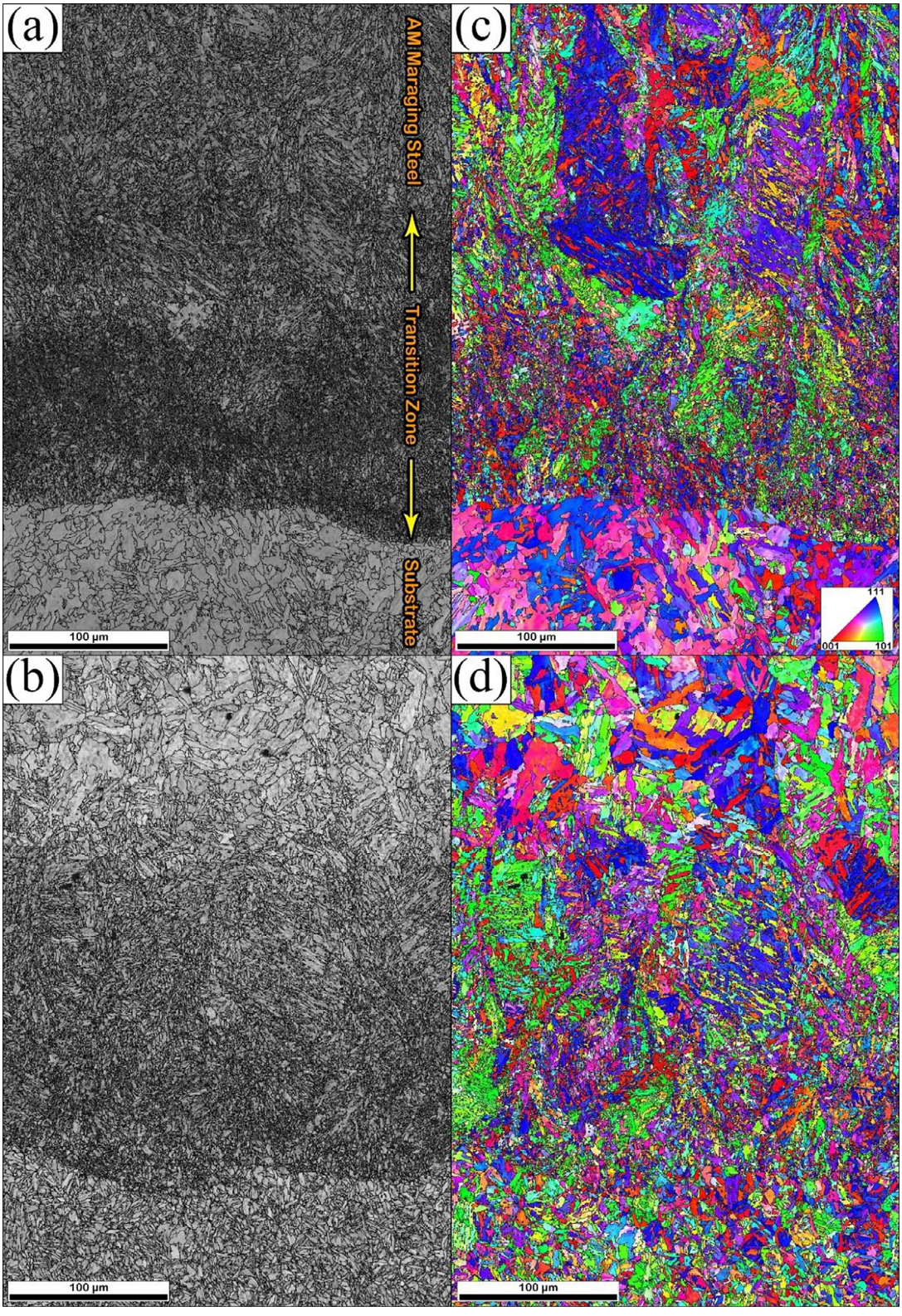

Fig. 8. Band contrast: a) AB b) HAT; BD-IPF map: c) AB d) HAT across the interface.

from low values of P20 to high values of MS1 across the interface. However, the HT treatment at 880 ˚C reversed the hardness profile, where a very hard substrate was obtained, followed by a drastic decrease in MS1 hardness. The HT temperature was extremely high to cause softening in the MS1. Despite the hardness increase in P20, the HT hardness profile is no longer favorable for mechanical performance since the MS1 side is abnormally softer than the substrate, which can cause early failure upon loading. Therefore, a complementary treatment should be carried out to level off the hardness profile across the interface. For this purpose, the HT treatment was followed by a treatment at 500 °C for 2 h. This heat treatment sequence (HAT) corrected the hardness variation and resulted in a relatively straightened hardness profile across the interface.

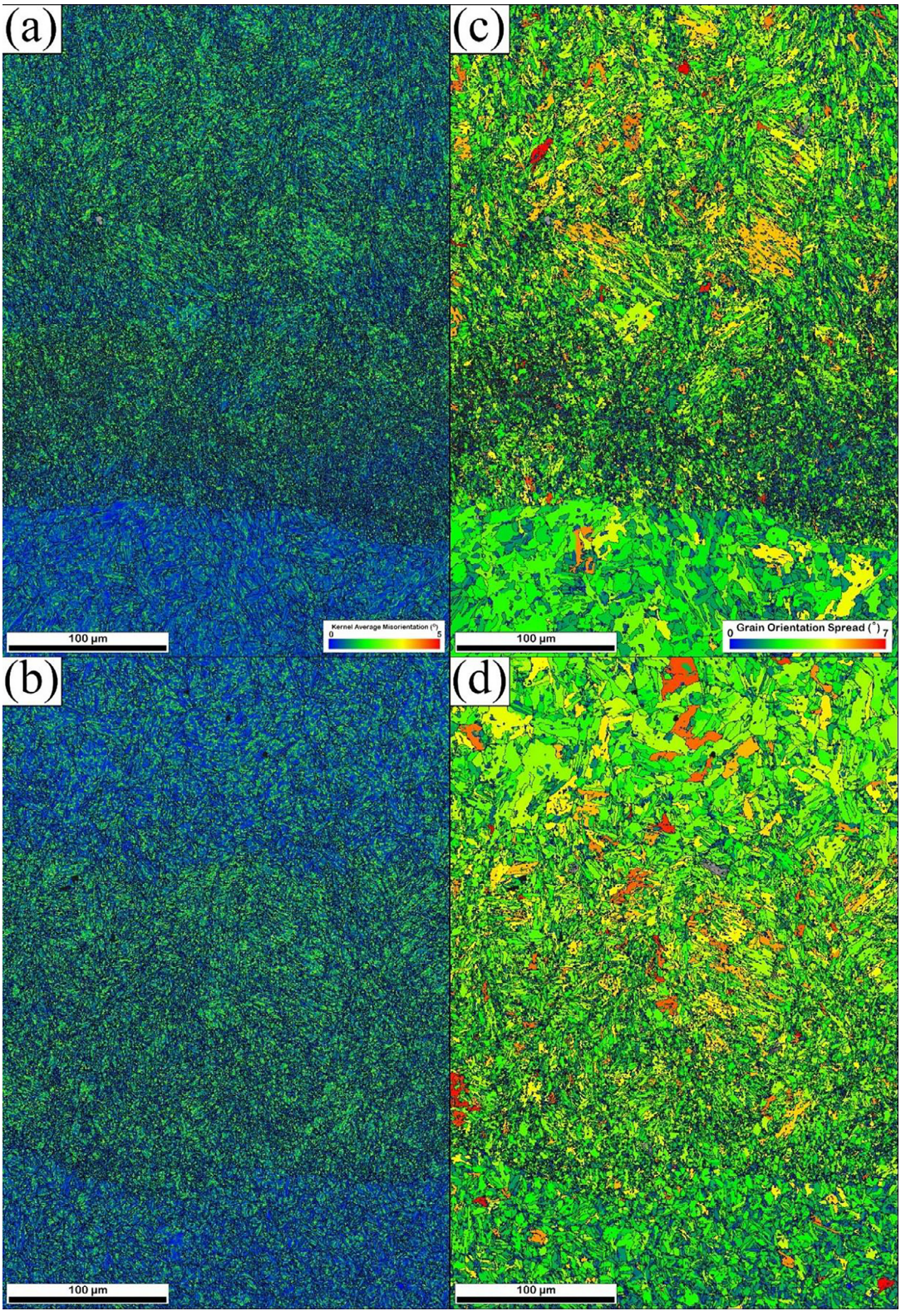

Fig. 9. KAM mapping: a) AB b) HAT; GOS mapping: c) AB d) HAT across the interface.

Thus, more uniform mechanical behavior can be expected in the HAT condition.

It was stated that the HAT treatment caused grain growth in MS1, while grain refinement occurred in P20. The following assessment was presented to understand better how the heat treatment caused the aforementioned morphological evolution in MS1 and P20. First, the PAGs were reconstructed for each step of the HAT sequence, and then they were compared with their original EBSD maps. The PAG maps can be regarded as representative microstructures at high temperatures. Fig. 14 indicates step-by-step morphological changes for both MS1 and P20 and clearly shows the evolution of grains in terms of grain size and shape during the HAT sequence. In addi-

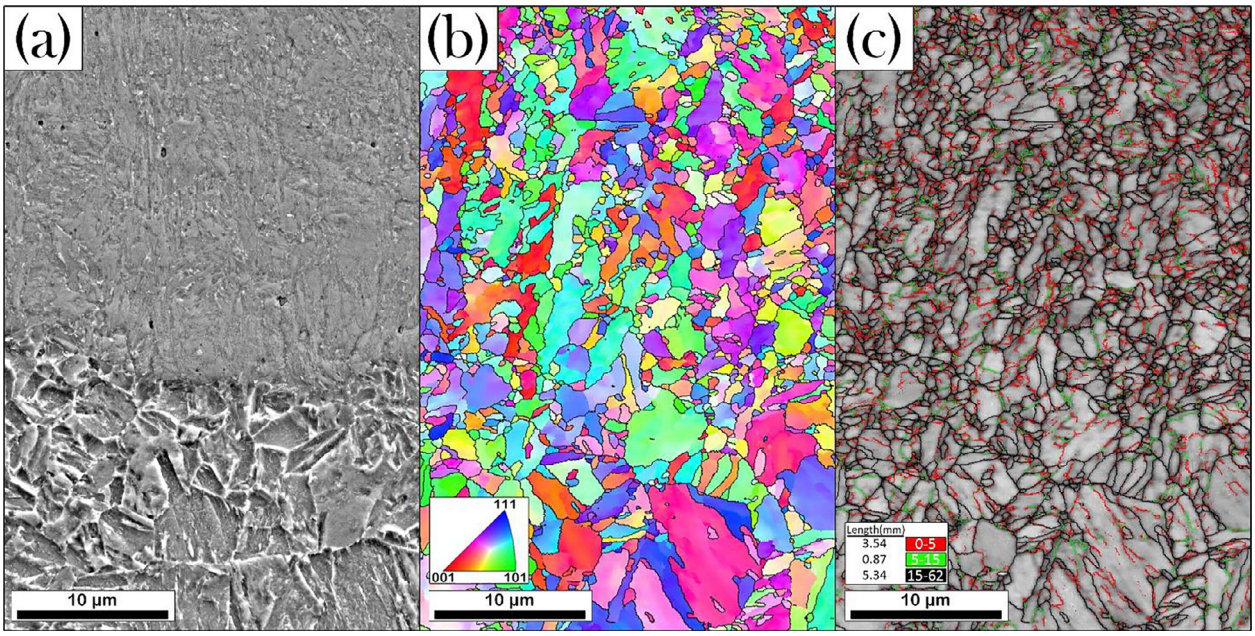

Fig. 10. a) SEM micrograph b) BD-IPF map c) grain boundary map across the interface at high magnification.

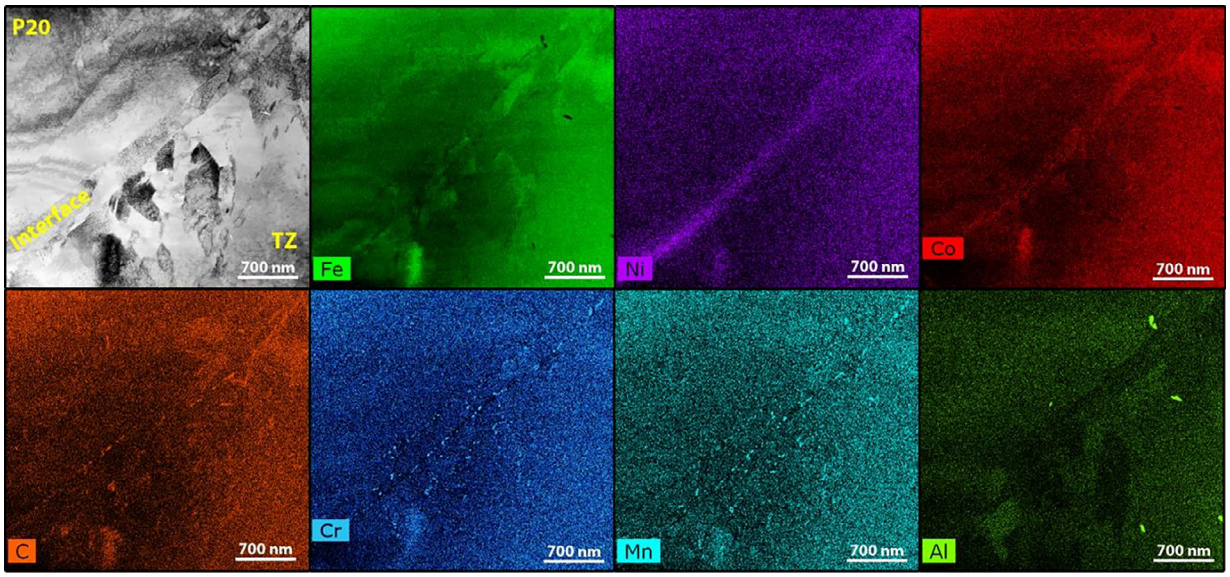

Fig. 11. STEM-EDS elemental analysis of HAT-interface.

tion, the effect of heating cycles are separately highlighted for each material.

In MS1, the HT treatment caused an abnormal grain growth by a factor of 15, where the as-built grain area of 98.49 μm^2 (step I) raised to 1527.20 μm^2 at 880 °C (step II), as shown in Fig. 14(a). Since this temperature is within the range of the solution temperature of maraging steels [62,63], the as-built grain boundaries and solidification cells dissolved, and more equiaxed austenite grains with coarser size appeared. The subsequent quenching turned the coarse austenitic morphology into a finer martensitic structure (step III). In the next step, the resultant PAG grain size was measured to be 567.17 μm^2 (step IV), which is much finer than the grain size at 880 °C. This can be related to the finer martensite structure of step III and lower aging temperature, which can lead to finer PAGs upon heating. Finally, coarser martensite grains (106.03 μm^2) were developed during cooling to room temperature (step V). The larger grain area of step V compared to step III can be attributed to a slower cooling rate of aging, resulting in a coarser martensite structure in MS1. Although the precipitation during aging can inhibit grain growth, the holding time of 2 h might not be sufficient to trigger this effect. In terms of grain geometry, the HT treatment successfully created more equiaxed grains (steps I-II); however, the martensite transformation during cooling resulted in more columnar grains (steps II-III and IV-V). This is mainly due to the martensite structure, in which columnar martensite packets were developed as the dominant microstructure.

Fig. 14(b) shows the corresponding step-by-step morphological map for P20. The first heating cycle from room temperature to 880 °C did not alter the grain sizes, and only a negligible grain growth occurred, where the grain area slightly raised from 160.29 μm^2 to 170.03 μm^2. On the other hand, the columnar grains of as-received P20 evolved to more equiaxed grains at this temperature since 92% of PAGs involved an aspect ratio of ≥ 0.33 (step II). The HT treatment rearranged the P20 grains along and dissolved the carbide precipitates. Upon quenching, a very

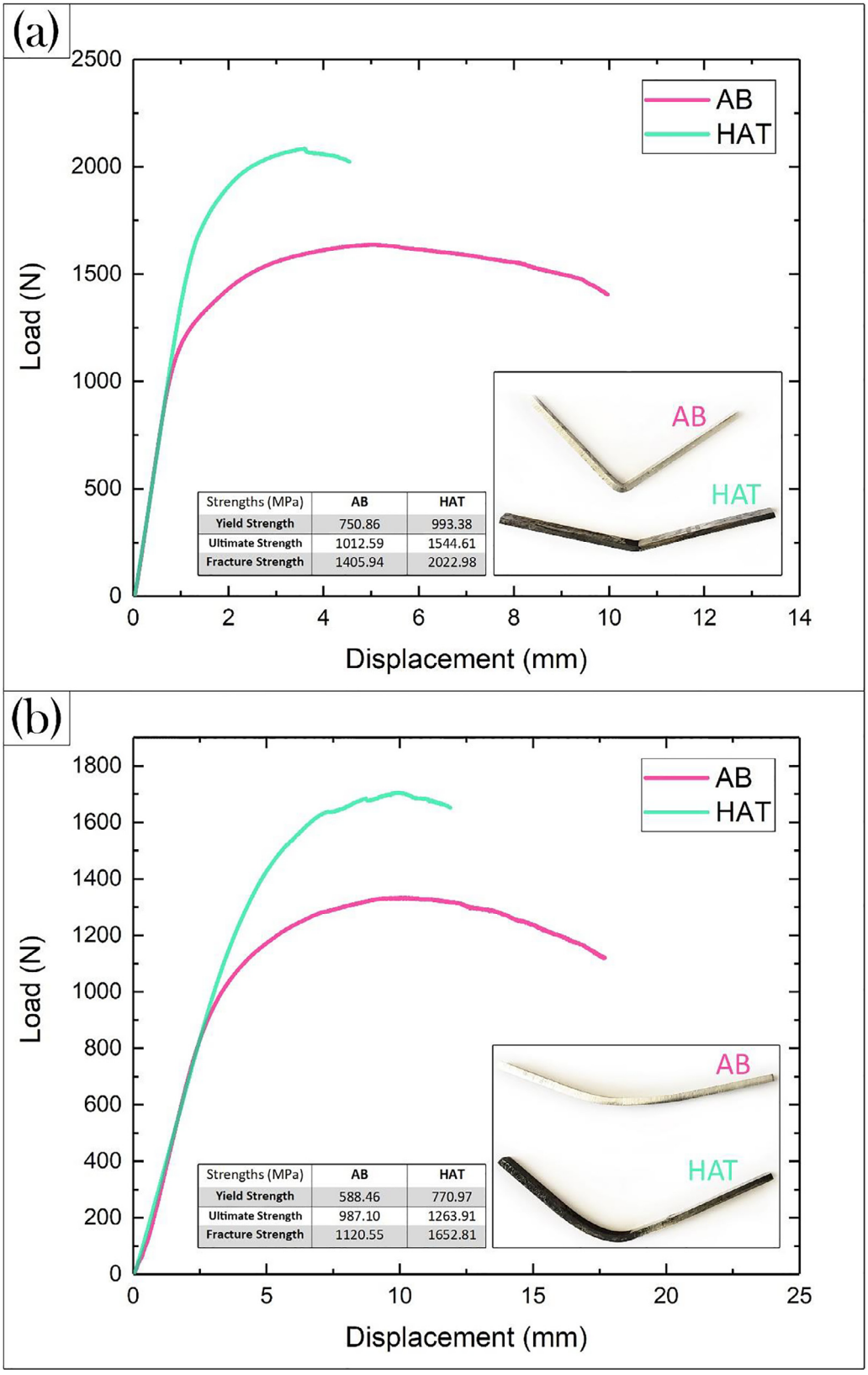

Fig. 12. Load-displacement profile for a) 3P bending b) 4P bending tests.

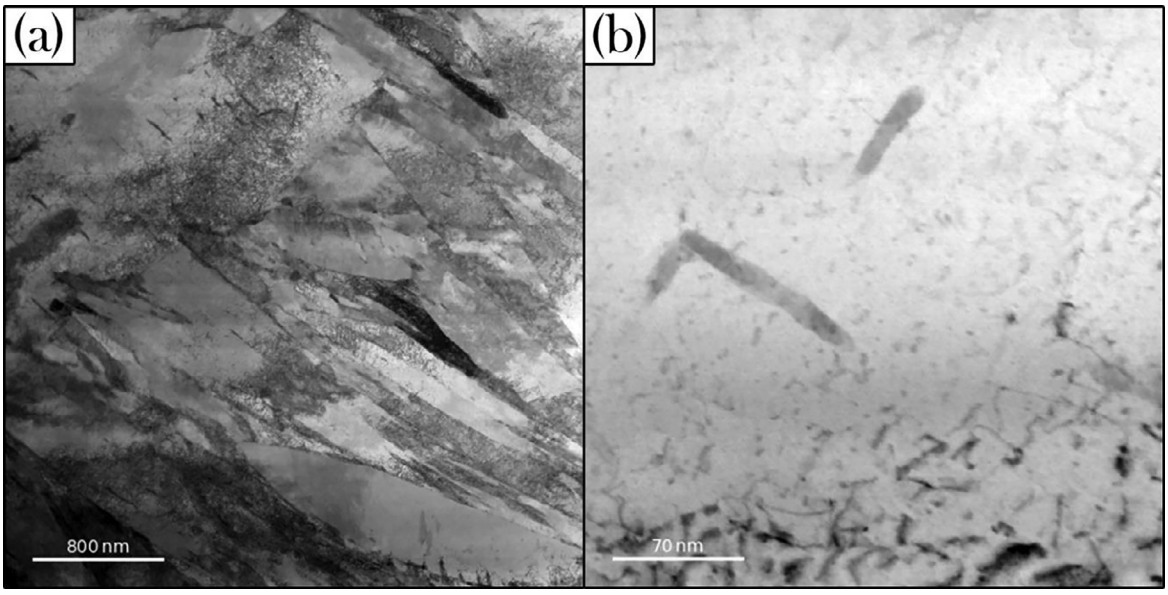

Fig. 13. STEM bright-field images showing the general microstructure and the dislocation arrangement in HAT-sample after the 4P bending test.

fine martensite structure was formed (Step III). Comparing steps I and III, a remarkable grain refinement can be seen as a result of the martensite transformation which led to very high hardness values of P20 in the HT condition. In the next heating cycle to 500 °C (step IV), finer PAGs were also constructed compared to 880 °C. Likewise, the finer martensitic grains of step III and lower aging temperature can cause smaller PAGs in step IV. In the final step V, the P20 grains evolved as small as the grains in step III, so the main contributor to the grain refinement is the HT treatment at 880 °C. Regarding the grain geometry, it seems that both heating cycles (steps I-II and III-IV) reformed the grains in equiaxed shapes, while the subsequent martensite transformation upon cooling resulted in more columnar grains. The grain refinement of P20 diminished the grain size difference between P20 and TZ and promoted an indistinguishable interface in the HAT condition. Moreover, lower hardness was achieved in the HAT condition. The treatment at 500 °C acted as a tempering treatment on P20 and encouraged stress relief in step IV. Subsequently, lower hardness values were measured in step V, which was favorable since a more uniform hardness profile was formed across the HAT-interface.

The PBF process involves intensive and localized heating followed by rapid solidification, so the grains can absorb residual stresses and contain high strains. In addition, the HAT sequence might affect the grains in this regard. Consequently, strain variation should be significant across the interface and plays an important role in the mechanical performance of the hybrid MS1-P20 steel. Therefore, quantitative strain analysis was carried out using GOS and KAM values, and the changes were evaluated before and after the HAT sequence. Fig. 15 compares the distribution of GOS misorientations for each area of the interface before and after the heat treatment. To distinguish the high-strain grains, a threshold of GOS > 2° was selected and used as the criteria to calculate the percentage of high-strain grains [16,64,65]. The as-received P20 contains the lowest GOS values, and only 29% of grains are high in strain. However, the HAT sequence raised this value to 39% for P20. Both TZ and MS1 areas are associated with higher values of GOS and contain 53% and 63% high-strain grains, respectively. The HAT sequence led to higher high-strain grains in TZ (62%), while the opposite trend occurred in MS1 (58%). Quantitative measurement of KAM-based misorientation is also included in Fig. 15, which simply shows the misorientation evolution of each zone across the interface. The average misorientation of P20 slightly increased during the HAT sequence with a minute increase from 0.64° to 0.72°. The same trend also occurred in TZ, where the average misorientation of 0.89° raised to 0.94°. KAM misorientation, however, reduced from 0.96° to 0.77° upon heat treatment in the MS1 area. This reduction can be seen in Fig. 9(b). Both GOS and KAM analyses revealed that the fluctuation of strain values tends to be subtle across the interface after heat treatment (HAT). This effect was also observed in Fig. 9(d).

The HAT sequence effectively modified the microstructure of MS1-P20 hybrid steel in terms of hardness, grain morphology, and strain values. As a result, the bending properties were also affected by this modification, as indicated in Fig. 12. The HAT sequence enhanced the ultimate strengths in three-point and four-point bending conditions by a factor of 1.53 and 1.28, respectively. The enhancement of bending strength can be highly entangled with the deformation mechanism of the hybrid steel during the bending tests.

The three-point bending samples were studied using the EBSD technique to correlate the bending deformation to the microstructure. Strain analysis was investigated across the interface and shown in Figs. 16 and 17 for AB- and HAT- samples, respectively. The 3P samples and the location of EBSD analysis were also presented in Figs. 16(a) and 17 (a) for AB and HAT conditions, respectively. In Figs. 16 and 17, the top and bottom indicate the areas with the highest compression and tension stresses, respectively. Fig. 16(b) illustrates the GOS mapping of the as-built specimen after the three-point bending test. This figure suggests that the P20 edges are highlighted in warm color, meaning that most strains are stored in the P20 edges, where the highest compression and tension stresses were applied in the top and bottom of the bending sample, respectively. The KAM mapping is also shown in Fig. 16(c), which can be considered as the distribution of dislocations throughout the sample. On the P20 side, the edges look saturated with KAM values indicating a high density of dislocations because of the stress conditions. In the middle of the bending sample, the variation of KAM seems identical to that of Figs. 9(a)-(c), showing lower strain values in P20 while higher values on the MS1 side. This is mainly attributed to stress conditions in which the least stress concentrated in the middle of the sample in the 3-point bending test.

The GOS mapping and KAM distribution were also extracted for the HAT-sample and presented in Figs. 17(b)-(c). In this condition, both maps evolved uniformly, and lower color contrast can be observed across the interface. The P20 edges are still areas of higher strains; however, the KAM contrast between the edges and the middle area seems less intense than the corresponding areas in Fig. 16. Therefore, the dislocations were distributed homogeneously in the HAT-sample.

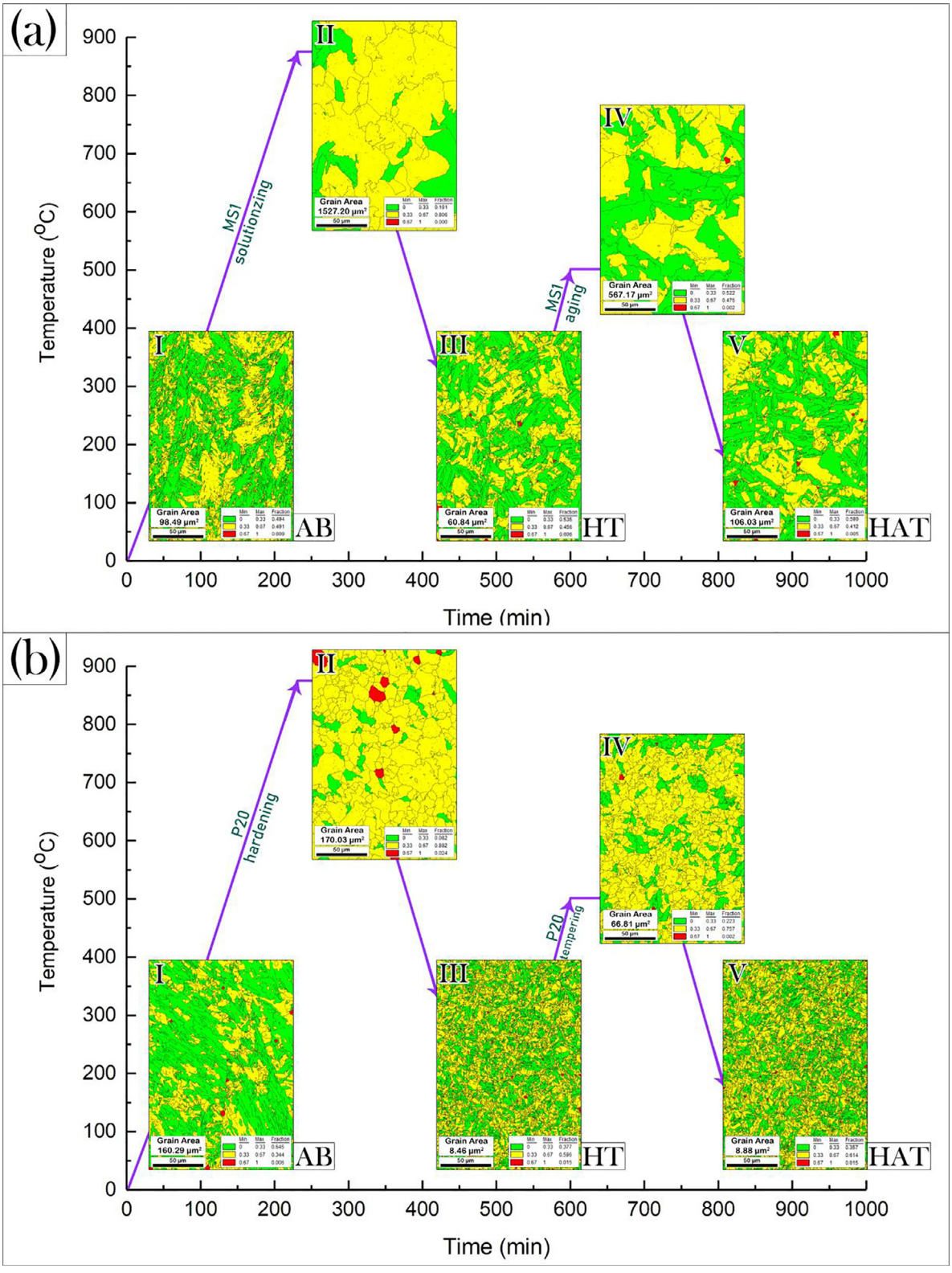

Fig. 14. Morphological variation of a) MS1 b) P20 during HAT sequence. It should be noted that II and IV maps have been reconstructed based on the EBSD maps of III and V, respectively.

The deformation mechanism can also be evaluated using the Schmid factor mapping. The {110}<111> and {112}<111> as the main slip systems of BCC and BCT crystallographic structures [66–68] were selected and used to extract the Schmid factors. Figs. 18(a)-(b) suggest that both slip systems were active and contributed to the deformation of the AB-sample. The average value of Schmid factor for {110}<111> and {112}<111> slip systems are 0.48 and 0.45, respectively. Although the Schmid factor was measured to be relatively identical for both slip systems, the {110}<111> slip system seems to be more active than the {112}<111> slip system in AB-sample. These values: however, were

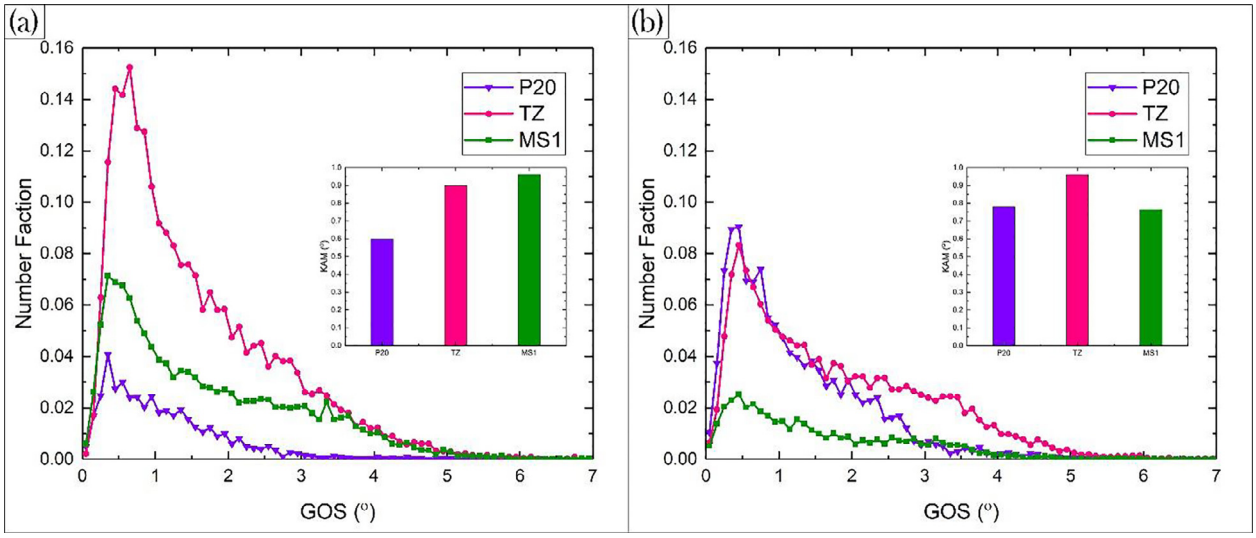

Fig. 15. GOS & KAM strain analysis of a) AB and b) HAT.

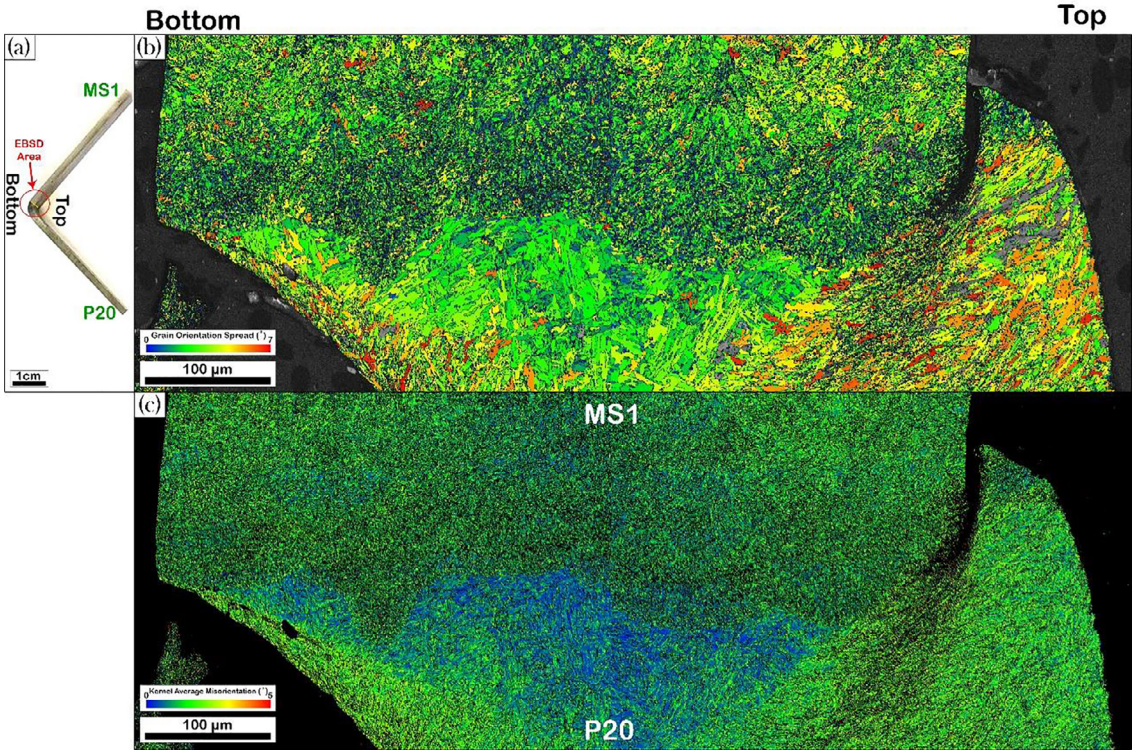

Fig. 16. Strain analysis of AB-interface after 3P bending: a) GOS b) KAM.

calculated to be 0.46 and 0.45 for the HAT-sample (See Figs. 19(a)-(b)). There is also a contrast between P20 and MS1 in the as-built condition, implying that the deformation activity is different between these two materials. The P20 side seems brighter than the MS1 side, which means the slip systems are relatively less active in P20 than in MS1. In HAT-sample, both slip systems exhibit indistinguishable mapping across the interface, and no contrast between P20 and MS1 sides can be observed. Therefore, uniform deformation occurred across the MS1-P20 hybrid steel in the HAT condition.

It was shown that the as-received P20 was weaker than the additive side in the AB-sample (see Fig. 2). Plastic deformation initiated from P20 at lower loading values. In the 3P bending test, the top and bottom of the MS1-P20 sample are the areas with the highest stresses, as indicated. So plastic deformation mainly occurred in the P20 edges. The dislocations were generated and moved in the slip systems; however, the P20 grains could not tolerate further movement of dislocations at some point, and the dislocations began to accumulate. Excessive accumulation of dislocations leads to the formation of voids, propagation of cracks in the edges, and finally, failure of the AB-sample. The dislocation accumulation is evident in Fig. 16(c) in the bottom and top edges of P20. This figure also proved that dislocations could not move and propagate to the middle of P20, and dislocations were blocked in the edges. Moreover, the P20 edges contain some green color grains in Fig. 18. This means that the slip systems had the lowest activity in these grains, which is well consistent with the impeded dislocation at the edges (see Fig. 16(c)). Therefore, the existence of the least active grains in high strain areas

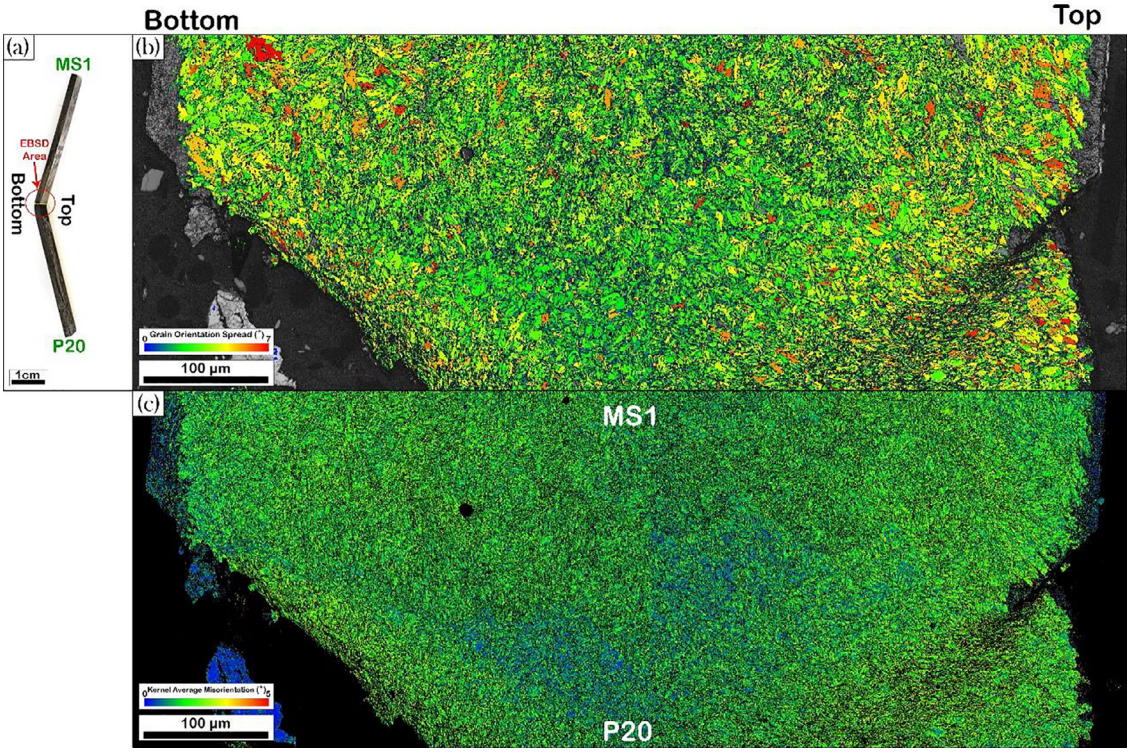

Fig. 17. Strain analysis of HAT-interface after 3P bending: a) GOS b) KAM.

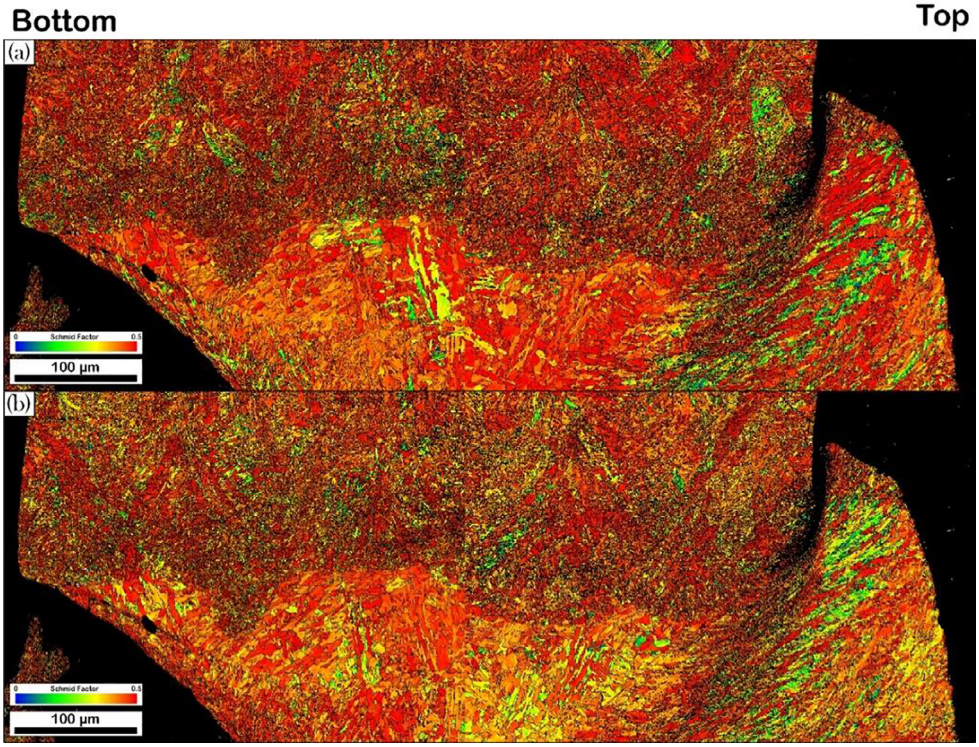

Fig. 18. Deformation maps of AB-interface after 3P bending: a) {110}<111> b) {112}<111> slip systems.

of the sample suggests that the as-received P20 grains possess very low deformability. The AB-sample consequently failed at a lower strength.

The KAM map evolved as a homogenous profile throughout the HAT-sample upon the HAT sequence. This is particularly important from the bottom to top areas of the sample, where the highest stresses were applied. Indeed, dislocations distributed more uniformly and hence had more mobility to move and propagate throughout the sample (see Fig. 17(c)). The uniform distribution of dislocations definitely indicates that the plastic deformation took place homogeneously in the HAT condition. This is well demonstrated in Fig. 19, where there is no contrast across the interface or from the bottom to top areas. Upon the HAT sequence, a comparable martensitic structure was developed between P20

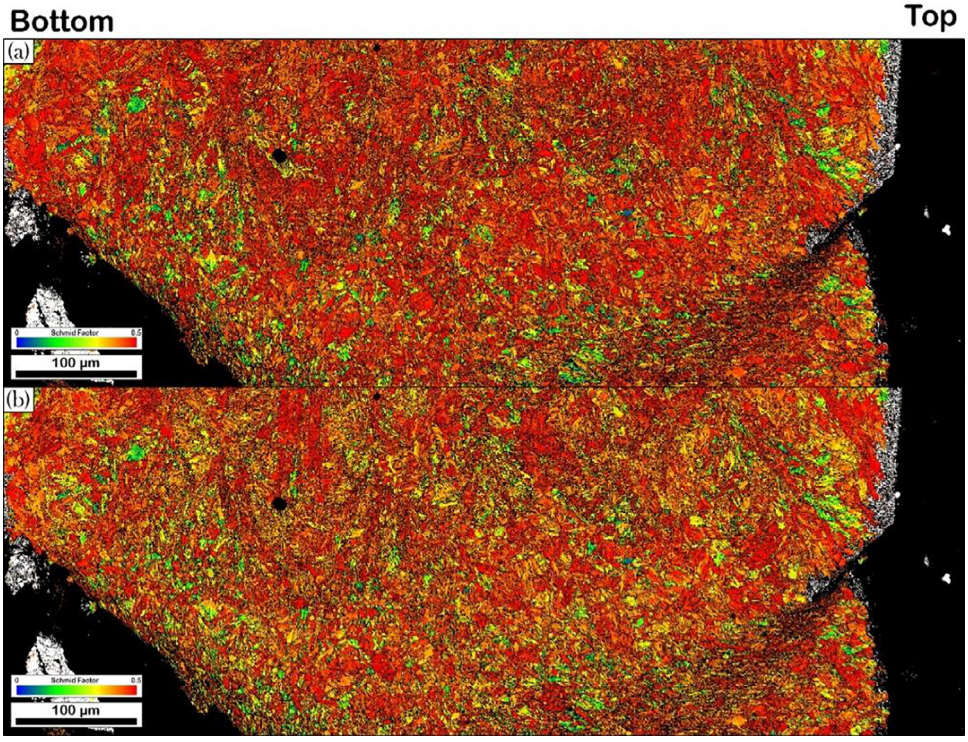

Fig. 19. Deformation maps of HAT-interface after 3P bending: a) {110}<111> b) {112}<111> slip systems.

and MS1, and the resultant interfacial microstructure generated identical hardness and strength on both sides of the interface. Therefore, the MS1-P20 hybrid steel featured monotonous deformation properties and exhibited higher strength under complex loading conditions of bending tests. Consequently, the MS1-P20 interface was favorably engineered using the HAT sequence.

5. Conclusion

The current research investigated the heat treatment and mechanical behavior of additively manufactured MS1-P20 hybrid steels under complex loading conditions. An effective heat treatment sequence was proposed, and the following outcomes were produced:

- The hardening treatment at 880 ˚C/1 hour followed by the aging treatment at 500 ˚C/2 h was designated as the HAT sequence. This heat treatment sequence generated the martensite phase on the P20 side and reformed the martensitic matrix of MS1.
- The HAT sequence caused two opposing grain evolutions: grain growth in MS1 and grain refinement in P20. This effect rearranged the grain morphology across the interface.
- Both AB- and HAT- samples consisted of three main zones, including P20, TZ, and MS1. And the interface was defined as the boundary between P20 and TZ. The AB-interface was clearly distinctive in EBSD maps; however, the HAT sequence removed this distinction and made a less distinguishable interface.
- The HAT-sample featured almost constant hardness properties across the interface, while wide fluctuation of hardness was detected in the AB-sample.
- The HAT sequence successfully homogenized the strain energy across the interface and promoted uniform deformation in bending conditions.
- The HAT-interface did not fail under 3P- and 4P- bending tests, and cracking initiated and grew with P20.
- The HAT-sample yielded and failed at higher bending strengths than the AB-sample. Thus this sequential heat treatment can be a practical approach to modifying MS1-P20 hybrid steel.

Declaration of Competing Interest

The authors declare that they have no known competing financial interests or personal relationships that could have appeared to influence the work reported in this paper.

Acknowledgments

The authors would like to thank Atlantic Canada Opportunities Agency (ACOA)-Atlantic Innovation Fund (AIF) project number 210414 and Mitacs Accelerate Program grant number IT10669 for providing sufficient funding to execute this work. The support from Brian Guidry and Vince Boardman at UNB-Mechanical Engineering for sample preparation and mechanical testing, and Dr. Douglas Hall and Steven Cogswell at UNB's Microscopy and Microanalysis Facility for SEM and EDS analyses are highly acknowledged.

References

[1] S. Chandrasekaran, S. Hari, M. Amirthalingam, Functionally graded materials for marine risers by additive manufacturing for high-temperature applications: experimental investigations, Structures 35 (May 2020) (2022) 931–938.
[2] R.B. Govindaraj, E. Junghans, I. Andersen, Y. ki Lim, P. Lindström, Additive manufactured marine component – Ni Al bronze propeller, Procedia Struct. Integr. 34 (2019) (2021) 20–25.
[3] K. Moeinfar, F. Khodabakhshi, S.F. Kashani-bozorg, M. Mohammadi, A.P. Gerlich, A review on metallurgical aspects of laser additive manufacturing (LAM): stainless steels, nickel superalloys, and titanium alloys, J. Mater. Res. Technol. 16 (2022) 1029–1068.
[4] S. Chandrasekaran, S. Hari, M. Amirthalingam, Wire arc additive manufacturing of functionally graded material for marine risers, Mater. Sci. Eng. A 792 (May) (2020) 139530.
[5] M.A.C. Gonzales, P. Kujala, Additive manufacturing of miniature marine structures for crashworthiness verification: a numerical revision, Appl. Ocean Res. 111 (April) (2021) 102653.
[6] M.A.G. Calle, M. Salmi, L.M. Mazzariol, M. Alves, P. Kujala, Additive manufacturing of miniature marine structures for crashworthiness verification: scaling technique and experimental tests, Mar. Struct. 72 (April) (2020) 102764.
[7] H. Monteiro, G. Carmona-Aparicio, I. Lei, M. Despeisse, Energy and material efficiency strategies enabled by metal additive manufacturing – A review for the aeronautic and aerospace sectors, Energy Reports 8 (2022) 298–305.

[8] B. Blakey-Milner, et al., Metal additive manufacturing in aerospace: a review, Mater. Des. 209 (2021) 110008.
[9] R. Alaghmandfard, et al., Characterization and statistical modeling of texture and microstructure evolution in dynamically fractured electron beam melted Ti-6Al-4b V, Materialia 21 (January) (2022) 101342.
[10] S. Dehgahi, et al., Texture evolution during high strain-rate compressive loading of maraging steels produced by laser powder bed fusion, Mater. Charact. 178 (March) (2021) 111266.
[11] V. Dehnavi, et al., Corrosion Behaviour of Electron Beam Melted Ti6Al4V: effects of Microstructural Variation, J. Electrochem. Soc. 167 (13) (2020) 131505.
[12] C. Dharmendra, B.S. Amirkhiz, A. Lloyd, G.D.J. Ram, M. Mohammadi, Wire-arc additive manufactured nickel aluminum bronze with enhanced mechanical properties using heat treatments cycles, Addit. Manuf. 36 (May) (2020) 101510.
[13] C. Dharmendra, K.P. Rice, B.S. Amirkhiz, M. Mohammadi, Atom probe tomography study of κ-phases in additively manufactured nickel aluminum bronze in as-built and heat-treated conditions, Mater. Des. 202 (2021) 109541.
[14] N. Hasani, et al., Laser powder bed fused Inconel 718 in stress-relieved and solution heat-treated conditions, Mater. Charact. 181 (October) (2021) 111499.
[15] S. Astafurov, et al., Electron-beam additive manufacturing of high-nitrogen steel: microstructure and tensile properties, Mater. Sci. Eng. A 826 (July) (2021) 141951.
[16] S.A.R. Shamsdini, et al., A relationship between the build and texture orientation in tensile loading of the additively manufactured maraging steels, Addit. Manuf. 41 (February) (2021) 101954.
[17] P. Durai Murugan, et al., A current state of metal additive manufacturing methods: a review, Mater. Today Proc. (2021) no. xxxx.
[18] X. Zhang, et al., Additive manufacturing of copper – H13 tool steel bi-metallic structures via Ni-based multi-interlayer, Addit. Manuf. 36 (April) (2020) 101474.
[19] L. Liu, Z. Zhuang, F. Liu, M. Zhu, Additive manufacturing of steel-bronze bimetal by shaped metal deposition: interface characteristics and tensile properties, Int. J. Adv. Manuf. Technol. 69 (9–12) (2013) 2131–2137.
[20] W.W. Wits, E. Amsterdam, Graded structures by multi-material mixing in laser powder bed fusion, CIRP Ann 70 (1) (2021) 159–162.
[21] A.G. Demir and B. Previtali, "Multi-material selective laser melting of Fe /Al-12Si components," vol. 11, pp. 8–11, 2017.
[22] M.G. Scaramuccia, A.G. Demir, L. Caprio, O. Tassa, B. Previtali, Development of processing strategies for multigraded selective laser melting of Ti6Al4V and IN718, Powder Technol. 367 (2020) 376–389.
[23] A. Ozsoy, E.B. Tureyen, M. Baskan, E. Yasa, Microstructure and mechanical properties of hybrid additive manufactured dissimilar 17-4 PH and 316 L stainless steels, Mater. Today Commun. 28 (April) (2021).
[24] M. Schneck, M. Horn, M. Schmitt, C. Seidel, G. Schlick, G. Reinhart, Review on additive hybrid- and multi-material-manufacturing of metals by powder bed fusion: state of technology and development potential, Prog. Addit. Manuf. 6 (4) (2021) 881–894.
[25] C.F. Tey, X. Tan, S.L. Sing, W.Y. Yeong, Additive manufacturing of multiple materials by selective laser melting: ti-alloy to stainless steel via a Cu-alloy interlayer, Addit. Manuf. 31 (November 2019) (2020) 1–16.
[26] A. Hadadzadeh, B.S. Amirkhiz, S. Shakerin, J. Kelly, J. Li, M. Mohammadi, Microstructural investigation and mechanical behavior of a two-material component fabricated through selective laser melting of AlSi10Mg on an Al-Cu-Ni-Fe-Mg cast alloy substrate, Addit. Manuf. 31 (June 2019) (2020).
[27] C. Dharmendra, S. Shakerin, M. Mohammadi, Metallurgical Assessment of Additive Manufactured Nickel Aluminum Bronze-316 L Stainless Steel Bimetallic Structure: effect of Deposit Geometry on the Interfacial Characteristics and Cracking, J. Mater. Eng. Perform. 30 (12) (2021) 8746–8762.
[28] M.H. Ghoncheh, et al., On the solidification characteristics, deformation, and functionally graded interfaces in additively manufactured hybrid aluminum alloys, Int. J. Plast. 133 (March) (2020).
[29] C. Dharmendra, S. Shakerin, G.D.J. Ram, M. Mohammadi, Wire-arc additive manufacturing of nickel aluminum bronze/stainless steel hybrid parts – Interfacial characterization, prospects, and problems, Materialia 13 (May) (2020).
[30] C. Tan, K. Zhou, W. Ma, L. Min, Interfacial characteristic and mechanical performance of maraging steel-copper functional bimetal produced by selective laser melting based hybrid manufacture, Mater. Des. 155 (2018) 77–85.
[31] J.N. Lagarinhos, S. Santos, G. Miranda, D. Afanso, R. Torcato, C. Santos, J.M. Oliveira, The inluence of surface finishing on laser heat treatments of a tool steel, Procedia CIRP 108 (2022) 839–844.
[32] Z. Cheng, S. Sun, X. Du, Q. Tang, J. Shi, X. Liu, Microstructural evolution of a FeCo15Cr14Ni4Mo3 maraging steel with high ductility prepared by selective laser melting, Mater. Today Commun. 31 (2022).
[33] Z. Mao, X. Lu, H. Yang, X. Niu, L. Zhang, X. Xie, Processing optimizaion, microstructure, mechanical properties and nanoprecipitation behavior of 18Ni300 maraging steel in selective laser melting, Mater. Sci. Engin. A 380 (2022).
[34] J. Song, Q. Tang, Q. Feng, Q. Han, S. Ma, H. Chen, F. Guo, R. Setchi, Effect of remelting processes on the microstructure and mechanical behaviours of 18Ni-300 maraging steel manufactured by selective laser melting, Mater. Charact. 184 (2022).
[35] T.H. Becker, Di. DImitrov, The achievable mechanical properties of SLM produced Maraging Steel 300 components, Rapid Prototyp. J. 22 (3) (2016) 487–494.
[36] E.A. Jägle, Z. Sheng, P. Kürnsteiner, S. Ocylok, A. Weisheit, D. Raabe, Comparison of maraging steel micro- and nanostructure produced conventionally and by laser additive manufacturing, Materials (Basel) 10 (1) (2017).
[37] A.T. Clare, et al., Alloy design and adaptation for additive manufacture, J. Mater. Process. Technol. 299 (June) (2021) 2022.
[38] Y. Bai, Y. Yang, D. Wang, M. Zhang, Influence mechanism of parameters process and mechanical properties evolution mechanism of maraging steel 300 by selective laser melting, Mater. Sci. Eng. A 703 (April) (2017) 116–123.
[39] S. Shakerin, A. Hadadzadeh, B.S. Amirkhiz, S. Shamsdini, J. Li, M. Mohammadi, Additive manufacturing of maraging steel-H13 bimetals using laser powder bed fusion technique, Addit. Manuf. 29 (June) (2019).
[40] Y. Bai, C. Zhao, Y. Zhang, H. Wang, Microstructure and mechanical properties of additively manufactured multi-material component with maraging steel on CrMn steel, Mater. Sci. Eng. A 802 (December 2020) (2021) 140630.
[41] J. Samei, et al., A hybrid additively manufactured martensitic-maraging stainless steel with superior strength and corrosion resistance for plastic injection molding dies, Addit. Manuf. 45 (January) (2021) 102068.
[42] O. Emadinia, J. Gil, R. Amaral, and R. Rocha, "Laser Deposited 18Ni300 Alloy Powder on 1045 Steel : effect of Passes and Preheating on Microstructure," 2022.
[43] S. Shakerin, M. Sanjari, B.S. Amirkhiz, M. Mohammadi, Interface engineering of additively manufactured maraging steel-H13 bimetallic structures, Mater. Charact. 170 (October) (2020).
[44] L. Kučerová, I. Zetková, Š. Jeníček, K. Burdová, Hybrid parts produced by deposition of 18Ni300 maraging steel via selective laser melting on forged and heat treated advanced high strength steel, Addit. Manuf. 32 (November) (2019) 2020.
[45] H. Azizi, et al., Metallurgical and mechanical assessment of hybrid additively-manufactured maraging tool steels via selective laser melting, Addit. Manuf. 27 (March) (2019) 389–397.
[46] S.L. Sing, L.P. Lam, D.Q. Zhang, Z.H. Liu, C.K. Chua, Interfacial characterization of SLM parts in multi-material processing: intermetallic phase formation between AlSi10Mg and C18400 copper alloy, Mater. Charact. 107 (2015) 220–227.
[47] B. Rankouhi, Z. Islam, F.E. Pfefferkorn, D.J. Thoma, Characterization of multi-material 316L-Hastelloy X fabricated via laser powder-bed fusion, Mater. Sci. Eng. A 837 (January) (2022) 142749.
[48] E.G. De Araujo, H. Pirgazi, M. Sanjari, M. Mohammadi, L.A.I. Kestensa, Automated reconstruction of parent austenite phase based on the optimum orientation relationship, J. Appl. Crystallogr. 54 (2021) 569–579.
[49] E. Gomes, L.A.I. Kestens, Fully automated orientation relationship calculation and prior austenite reconstruction by random walk clustering, IOP Conf. Ser. Mater. Sci. Eng. 82 (1) (2015).
[50] S.T. Methods, Standard Test Methods for Bend Testing of Material for Ductility 1, Current 03 (February) (1998) 1–7.
[51] G.E. Totten, Steel Heat Treatment Metallurgy and Technologies, CRC Press, 2007.
[52] A.S.M. Authors, Heat treating, ASM Int 4 (10) (Oct. 1991).
[53] G. Yan, S. Lu, M. Zhang, J. Wang, X. Yang, Z. Zhang, J. Gu, C. Li, Wear and corrosion behavior of P20 steel surface modified by gas nitriding with laser surface engineering, Appl. Surf. Sci. 530 (2020).
[54] H. Hoseiny, F.G. Caballero, R. M'Saoubi, B. Högman, J. Weidow, H.O. Andrén, The Influence of Heat Treatment on the Microstructure and Machinability of a Prehardened Mold Steel, Metall. Mater. Trans. A Phys. Metall. Mater. Sci. 46 (5) (2015) 2157–2171.
[55] M. Rout, R. Ranjan, S.K. Pal, S.B. Singh, EBSD study of microstructure evolution during axisymmetric hot compression of 304LN stainless steel, Mater. Sci. Eng. A 711 (July 2017) (2018) 378–388.
[56] C. Wang, Y. Yu, J. Yu, Y. Zhang, Y. Zhao, Q. Yuan, Microstructure evolution and corrosion behavior of dissimilar 304/430 stainless steel welded joints, J. Manuf. Process. 50 (December 2019) (2020) 183–191.
[57] V. Khademi, T.R. Bieler, C.J. Boehlert, On the correlation between plastic strain and misorientation in polycrystalline body-centered-cubic microstructures with an emphasis on the grain size, loading history, and crystallographic orientation, Int. J. Plast. 146 (August) (2021) 103084.
[58] Y. Zhang, Q. Chang, Y. Shao, X. Guo, Assessment of the creep damage in HR3C steel using the misorientation parameters derived from EBSD technique, Mater. Lett. 306 (September 2021) (2022).
[59] X. Li, A. Ramazani, U. Prahl, W. Bleck, Quantification of complex-phase steel microstructure by using combined EBSD and EPMA measurements, Mater. Charact. 142 (May) (2018) 179–186.
[60] U. Mayo, N. Isasti, D. Jorge-Badiola, J.M. Rodriguez-Ibabe, P. Uranga, An EBSD-based methodology for the characterization of intercritically deformed low carbon steel, Mater. Charact. 147 (September 2018) (2019) 31–42.
[61] S.A.R. Shamsdini, et al., A relationship between the build and texture orientation in tensile loading of the additively manufactured maraging steels, Addit. Manuf. 41 (March) (2021) 101954.
[62] F.F. Conde, et al., Effect of thermal cycling and aging stages on the microstructure and bending strength of a selective laser melted 300-grade maraging steel, Mater. Sci. Eng. A 758 (April) (2019) 192–201.
[63] Y. Bai, D. Wang, Y. Yang, H. Wang, Effect of heat treatment on the microstructure and mechanical properties of maraging steel by selective laser melting, Mater. Sci. Eng. A 760 (June) (2019) 105–117.
[64] Y.J. Ban, et al., EBSD analysis of hot deformation behavior of Cu-Ni-Co-Si-Cr alloy, Mater. Charact. 169 (May) (2020).
[65] N. Sayyar, M. Shamanian, B. Niroumand, J. Kangazian, J.A. Szpunar, EBSD observations of microstructural features and mechanical assessment of INCOLOY 825 alloy/AISI 321 stainless steel dissimilar welds, J. Manuf. Process. 60 (September) (2020) 86–95.
[66] S. Nambu, M. Michiuchi, Y. Ishimoto, K. Asakura, J. Inoue, T. Koseki, Transition in deformation behavior of martensitic steel during large deformation under uniaxial tensile loading, Scr. Mater. 60 (4) (2009) 221–224.
[67] K.H. Ryou, S. Nambu, T. Koseki, Effect of carbon content on selection of slip system during uniaxial tensile deformation of lath martensite, Mater. Sci. Eng. A 777 (November 2019) (2020) 139090.
[68] M. Michiuchi, S. Nambu, Y. Ishimoto, J. Inoue, T. Koseki, Relationship between local deformation behavior and crystallographic features of as-quenched lath martensite during uniaxial tensile deformation, Acta Mater 57 (18) (2009) 5283–5291.